

# Linear Polarization of the 21 cm Line from the Epoch of Reionization

BOHUA LI,<sup>1</sup> JIANRONG TAN,<sup>1,2</sup> AND YI MAO<sup>1</sup>

<sup>1</sup>*Department of Astronomy, Tsinghua University, Beijing, 100084, China*

<sup>2</sup>*Department of Physics & Astronomy, University of Pennsylvania, 209 South 33rd Street, Philadelphia, PA 19104, USA*

## ABSTRACT

The 21 cm linear polarization due to Thomson scattering off free electrons can probe the distribution of neutral hydrogen in the intergalactic medium during the epoch of reionization, complementary to the 21 cm temperature fluctuations. Previous study (Babich & Loeb 2005) estimated the strength of polarization with a toy model and claimed that it can be detected with 1-month observation of the Square Kilometre Array (SKA). Here we revisit this investigation with account of nonlinear terms due to inhomogeneous reionization, using seminumerical reionization simulations to provide the realistic estimation of the 21 cm TE and EE angular power spectra ( $C_\ell^{\text{TE}}$  and  $C_\ell^{\text{EE}}$ ). We find that (1) both power spectra are enhanced on sub-bubble scales but suppressed on super-bubble scales, compared with previous results; (2)  $C_\ell^{\text{TE}}$  flips its sign at  $\ell \simeq 50$ , which can probe the H I bias at large scales; (3) the ratios of the power spectrum to its maximum value during reionization at a given  $\ell$ , i.e.  $C_\ell^{\text{TE}}/C_{\ell,\text{max}}^{\text{TE}}$  and  $C_\ell^{\text{EE}}/C_{\ell,\text{max}}^{\text{EE}}$ , show robust correlations with the global ionized fraction. However, measurement of this signal will be very challenging not only because the overall strength is weaker than the sensitivity of SKA, but also because Faraday rotation due to Galactic and extragalactic magnetic fields significantly modifies the observed polarization. Nevertheless, it may still be possible that the 21 cm linear polarization signal may be detected through other approaches, e.g. its cross-correlation with other probes.

**Keywords:** Reionization (1383), H I line emission (690), Radio interferometry (1346), Intergalactic medium (813), Large-scale structure of the universe (902), Two-point correlation function (1951)

## 1. INTRODUCTION

The epoch of reionization (EoR) is a major phase transition of the Universe, during which the neutral hydrogen in the intergalactic medium (IGM) is heated and ionized by ultraviolet and X-ray photons from the first luminous objects. The process of cosmic reionization involves the formation of the large-scale structure and the rich astrophysics associated with the formation of first luminous objects. Current constraints on the EoR (Bouwens et al. 2015; Robertson et al. 2015; Finkelstein et al. 2019) are from robust but indirect probes, e.g., the observations of high-redshift quasar spectra (e.g., Fan et al. 2006; McGreer et al. 2015; Becker et al. 2015), and the electron scattering optical depth to the cosmic microwave background (CMB) (Planck Collaboration et al.

2020), in the sense that these probes are only sensitive to some, but not all, information of the EoR.

The most promising, direct, avenue of probing the EoR is the intensity mapping of the redshifted 21 cm line due to the hyperfine transition of atomic hydrogen (e.g., Pritchard & Loeb 2012), because the 21 cm tomography can map the distribution of neutral hydrogen (H I) for a broad range of redshifts along the light cone. This tomographic mapping, which reveals the global history and morphological structure of cosmic reionization, contains a wealth of information regarding the structure formation of the Universe (e.g., Scott & Rees 1990; McQuinn et al. 2006; Mao et al. 2008; Chen et al. 2019), and the properties of the first galaxies and quasars as the source of reionization (e.g., Ahn et al. 2015; Dixon et al. 2016).

The next decades will be the golden age for the 21 cm observations. Albeit still under debate, the EDGES experiment (Bowman et al. 2018), a global 21 cm experiment with a single dipole, claimed to have detected,

for the first time, the absorption feature in the global 21 cm brightness temperature during the cosmic dawn, the epoch when first galaxies begin to form. On the other hand, the next-generation radio interferometric arrays, including the Hydrogen Epoch of Reionization Array (HERA) (DeBoer et al. 2017) and the Square Kilometre Array (SKA) (Koopmans et al. 2015), promise to measure the statistical fluctuations of the 21 cm signal. Furthermore, the SKA will be sensitive enough to implement the 21 cm imaging.

The major efforts in the 21 cm modeling and data analysis (e.g., Madau et al. 1997; Furlanetto et al. 2004a; Morales & Hewitt 2004; Lidz et al. 2008; Hoffmann et al. 2019; Liu & Shaw 2020) have hitherto focused on the total intensity (i.e. Stokes parameter  $I$ ) of the 21 cm brightness temperature. However, the polarization of the 21 cm radiation field (i.e. Stokes parameter  $Q$ ,  $U$  and  $V$ ), as a complementary probe to the 21 cm temperature field, also contains independent information of the EoR. In fact, radio interferometers, as constructed by pairs of orthogonal dipole antennae, can be sensitive to the polarization information after careful calibration (Liu & Shaw 2020). Thorough investigations of the 21 cm polarization signal, therefore, are worthwhile in order to obtain additional science returns from the interferometric observations. This paper is dedicated to the 21 cm *linear* polarization (i.e. Stokes parameter  $Q$  and  $U$ ) from the EoR. Note that the circular polarization (i.e. Stokes parameter  $V$ ) of the 21 cm signal can also be produced through some mechanisms, e.g. the Zeeman splitting of the triplet state by local magnetic fields (Cooray & Furlanetto 2005), and the splitting induced by the CMB quadrupole during the dark ages (Hirata et al. 2018; Ji et al. 2021). However, the 21 cm circular polarization signal is subdominant during the EoR, and therefore not the focus of this paper.

Babich & Loeb (2005, hereafter BL05) pioneered the study of the 21 cm linear polarization signal, and discussed two categories of production mechanisms — intrinsic and secondary mechanisms. In principle, anisotropic Ly $\alpha$  pumping can produce a small signal of linear polarization intrinsically, i.e. at the time of emission of the 21 cm signal. The dominant effect, however, is due to the Thomson scattering of 21 cm photons off free electrons during the EoR. In analogy with the CMB polarization, the 21 cm radiation, even if unpolarized at the time of emission, will become partially linearly polarized when the scattering electrons see a quadrupole anisotropy in the temperature fluctuations, so this effect was called a secondary mechanism. In particular, for scalar perturbations, Thomson scattering only induces *E*-mode polarization due to symmetry argument.

BL05 studied the anisotropy of the 21 cm *E*-mode polarization and derived the EE and TE angular power spectra. As the first study of this subject, there are several limitations in their paper, as follows. (1) On the theoretical modeling, they only included the linear components in the power spectrum, and employed a simple ansatz for ionization power spectrum. As a result, their results may misestimate the signal on all scales. (2) On the observational side, their estimate of the instrumental noise, particularly its scale-dependence, was oversimplified. They forecast that the 21 cm TE power spectrum could be detected by the SKA with 1-month integration time. This forecast might be overly optimistic.

In this paper, we will revisit the formalism for the 21 cm linear polarization from the EoR, taking into account the nonlinear effect due to inhomogeneous reionization, and estimate the polarization signal with the realistic modeling of ionization power spectrum using the seminumerical simulation results. The formalism is kept in terms of the angular power spectrum,  $C_\ell$ , instead of the power spectrum,  $P(\vec{k})$ , since the former approach is more adapted to multifrequency studies and wide-field surveys (Zaldarriaga et al. 2004; Datta et al. 2007; Liu et al. 2016). We will investigate new features in the polarization angular power spectra, which may be used for constraining reionization. On the other hand, we will also discuss the foregrounds, systematics, and detection prospects of the polarization signal by the upcoming SKA telescope.

Note that in addition to the mechanisms that produce the linear polarization signal, Faraday rotation (FR) (e.g., Burn 1966) and gravitational lensing are able to convert the *E*-mode polarization into *B*-mode polarization during the propagation of light. In particular, FR, as induced by intervening Galactic and extragalactic magnetic fields along each line of sight, can be a substantial effect at low frequencies that poses a challenge to the measurement of the 21 cm polarization signal (De & Tashiro 2014). Nevertheless, futuristic broadband polarization surveys (e.g., using the Phase 1 of SKA-Mid) may be capable of mapping the Faraday depth with high precision (Heald et al. 2020), using analysis tools like Faraday rotation measure (RM) synthesis (Brentjens & de Bruyn 2005; Hutschenreuter & Enßlin 2020; O’Sullivan et al. 2020) and machine learning (Brown et al. 2019), which may allow for the reconstruction of the 21 cm polarization signal from the EoR. While a detailed treatment of this effect is beyond the scope of this paper, we will briefly discuss the FR effect.

The rest of this paper is organized as follows. In §2, we reformulate the angular power spectra of the 21 cm linear polarization signal, based on a fully relativistic

framework, while leaving the detailed account of this formalism and approximations to Appendix A and B. We then describe the EoR modeling and simulations in §3 which provide the initial source fields for the 21 cm signal. In §4, we present the numerical results and discuss their cosmological implications. We briefly discuss the observational prospects of the polarization signal in §5, and make concluding remarks in §6.

## 2. THE 21 CM LINEAR POLARIZATION

We derive the angular power spectra of the 21 cm linear polarization signal from Thomson scattering in this section.

### 2.1. Temperature anisotropy

For the interest of this paper, the concept of observers extends to fictitious ones such as free electrons on the photon path – when the 21 cm photons are scattered off those intervening free electrons, the electrons are “observing” the 21 cm radiation. We consider such “observers” on the past light cone of the present-day Earth labeled by their *relative redshift*  $z_{\text{obs}}$  between the “observers” and the Earth today,  $1 + z_{\text{obs}} = \nu_{\text{obs}}/\nu_{\text{obs},0}$ , where  $\nu_{\text{obs}}$  and  $\nu_{\text{obs},0}$  are the radiation frequencies seen by the “observer” and on the Earth today, respectively. For a fixed observer, the location of 21 cm emission events is labeled by FLRW coordinates  $(t_{\text{em}}, \vec{x} + \vec{r})$ .  $\vec{x}$  is the location of the observer and  $\vec{r} \equiv -r\hat{n}$ <sup>1</sup>. The conformal Newtonian gauge is adopted in this paper and the conformal time denoted as  $\eta$ . We also define a gauge-independent time variable, the cosmic time  $\bar{\eta}_{z_{\text{cos}}}$  which in the background FLRM model corresponds to cosmological redshift  $z_{\text{cos}}$ ,  $a(\bar{\eta}_{z_{\text{cos}}}) \equiv 1/(1 + z_{\text{cos}})$ .

The fundamental observable in 21 cm radiation for an “observer” is the differential 21 cm brightness temperature along a line of sight (LoS) per observed frequency bin,  $\delta T_{\text{b}}(\nu_{\text{obs}}, \hat{n})$ , generally written as

$$\delta T_{\text{b}}(\nu_{\text{obs}}, \hat{n}) = \left[ \frac{T_{\text{s}}^g}{1 + z} - T_{\text{CMB}}^{\text{obs}}(\hat{n}) \right] (1 - e^{-\tau_{\nu_{\text{obs}}}}), \quad (1)$$

where  $T_{\text{s}}^g$  is the spin temperature of the H I gas<sup>2</sup> (assuming single transition event along the LoS),  $1 + z = \nu_{21}/\nu_{\text{obs}}$  is the *relative redshift*<sup>3</sup> between the emission and the “observer”, and  $T_{\text{CMB}}^{\text{obs}}(\hat{n})$  is the CMB temperature along the LoS as seen by the “observer”.  $\nu_{21} = 1420$

MHz is the rest-frame frequency of the 21 cm transition.  $\tau_{\nu_{\text{obs}}}$  is the 21 cm optical depth at the observed frequency.

Before showing the 21 cm temperature anisotropy for such an “observer”, we briefly clarify all the approximations we make in this paper. For 21 cm signals from the EoR, we reasonably assume the optically-thin, post-heating, quasi-linear regime and refer readers to the details of these assumptions in Appendix A.1. Furthermore, the 21 cm signal from a fixed redshift (Eq. [1]) is subject to the light-cone (LC) effect. In this paper we will neglect the LC effect for the EoR signal, evaluating it at the ensemble-averaged location of the emission,  $(\bar{\eta}_{z_{\text{em}}}, \vec{x} - s\hat{n})$ , where  $1 + z_{\text{em}} \equiv (1 + z)(1 + z_{\text{obs}}) = 1/\langle a(\eta_{\text{em}}) \rangle$  and  $s \equiv \int_{z_{\text{obs}}}^{z_{\text{em}}} c d\tilde{z}/H(\tilde{z}) = c(\bar{\eta}_{z_{\text{obs}}} - \bar{\eta}_{z_{\text{em}}}) = \langle r(\hat{n}, z) \rangle$ <sup>4</sup>. We will only consider the dominant correction to the signal due to the redshift-space distortion (RSD). Justification of this treatment can be found in Appendix A.2.

The expression for the 21 cm brightness temperature with the observed frequency  $\nu_{\text{obs}}$  along the direction of  $\hat{n}$  as seen by the “observer” at  $(\eta_{\text{obs}}, \vec{x})$  is

$$\begin{aligned} \delta T_{\text{b}}(\eta_{\text{obs}}, \vec{x}, \nu_{\text{obs}}, \hat{n}) &\equiv T_0(z) \psi(\eta_{\text{obs}}, \vec{x}, \nu_{\text{obs}}, \hat{n}) \\ &\approx T_0(z) \bar{x}_{\text{HI},m}(z_{\text{em}}) \left( 1 + \delta_{\text{HI}} \right) \left( 1 - \frac{1}{\mathcal{H}} \frac{\partial v_{\parallel}}{\partial r} \right) \\ &\approx T_0(z) x_{\text{HI}} \left( 1 + \delta - \frac{1}{\mathcal{H}} \frac{\partial v_{\parallel}}{\partial r} \right). \end{aligned} \quad (2)$$

Here  $\delta_{\text{HI}}$  is the neutral hydrogen density fluctuations. In this expression, the terms responsible for the global signal include the *mass-weighted* average neutral fraction,  $\bar{x}_{\text{HI},m} \equiv \bar{n}_{\text{HI}}/\bar{n}_{\text{H}}$ , and the dimensional factor  $T_0$ ,

$$T_0(z) \equiv \frac{3c^3 A_{10} T_{21} \bar{n}_{\text{H}}(z_{\text{em}})}{32\pi \nu_{21}^3 (1 + z) H(z_{\text{em}})}, \quad (3)$$

where  $A_{10} = 2.85 \times 10^{-15} \text{ s}^{-1}$  is the 21 cm spontaneous emission rate,  $T_{21} \equiv h\nu_{21}/k_{\text{B}}$ , and  $\bar{n}_{\text{H}}(z_{\text{em}}) = (3\Omega_{\text{b}} H_0^2 X_{\text{P}}/8\pi G m_{\text{H}}) (1 + z_{\text{em}})^3$ , ( $X_{\text{P}}$  is the cosmic hydrogen mass abundance and  $m_{\text{H}}$  is the mass of atomic hydrogen). The global 21 cm brightness temperature (the ensemble-averaged value of the monopole) is then given by

$$\begin{aligned} \delta \bar{T}_{\text{b}}(\nu_{\text{obs}}) &= T_0(z) \bar{x}_{\text{HI},m}(z_{\text{em}}) = \frac{3c^3 A_{10} T_{21} \bar{n}_{\text{HI}}(z_{\text{em}})}{32\pi \nu_{21}^3 (1 + z) H(z_{\text{em}})} \\ &\approx (27 \text{ mK}) \left( \frac{\Omega_{\text{b}} h^2}{0.022} \right) \sqrt{\frac{0.14}{\Omega_{\text{m}} h^2}} \frac{1 + z_{\text{em}}}{10} \bar{x}_{\text{HI},m}(z_{\text{em}}). \end{aligned} \quad (4)$$

<sup>1</sup> We do not consider the evolution of the ray direction along the photon geodesic so that it is always along  $\hat{n}$ .

<sup>2</sup> In this paper the superscript ‘g’ denotes quantities in the locally inertial rest frame of the gas.

<sup>3</sup>  $z$  should not be confused with the cosmological redshift of the observer or that of the emitting gas in this paper.

<sup>4</sup> To exactly account for the LC anisotropy, however, one must resort to full numerical schemes (e.g., Mao et al. 2012; Mondal et al. 2018; Chapman & Santos 2019).

As for the fluctuations, all variables on the right-hand side of Eq. (2) are evaluated at  $(\bar{\eta}_{z_{\text{em}}}, \vec{x} - s\hat{n})$ <sup>5</sup>:  $\delta$  is the gauge-dependent matter overdensity (the baryon distribution is assumed to closely follow that of the total matter),  $x_{\text{HI}}$  is the local neutral fraction, and the LoS velocity gradient term,  $(1/\mathcal{H})(\partial v_{\parallel}/\partial r)$ , accounts for the RSD effect ( $v_{\parallel} \equiv \vec{v} \cdot \hat{r} = -\vec{v} \cdot \hat{n}$  is the LoS projection of the H I peculiar velocity at emission and  $\mathcal{H} \equiv aH$  is the conformal Hubble parameter). The RSD term is small in the quasi-linear regime,  $|(1/\mathcal{H})(\partial v_{\parallel}/\partial r)| \sim |\delta| \ll 1$ .

The dimensionless brightness temperature,  $\psi$ , is defined in Eq. (2). Its fluctuations are defined as  $\Theta(\eta_{\text{obs}}, \vec{x}, \nu_{\text{obs}}, \hat{n}) \equiv \delta T_{\text{b}}(\eta_{\text{obs}}, \vec{x}, \nu_{\text{obs}}, \hat{n})/\delta T_{\text{b}}(\nu_{\text{obs}}) - 1$ . Transforming into Fourier space and taking into account the linear-theory relation  $\vec{v}(\eta, \vec{k}) = i(\vec{k}/k)\mathcal{H}(\eta)\delta(\eta, \vec{k})$  during the matter-dominated era (Bharadwaj & Ali 2004), we obtain

$$\Theta(\eta_{\text{obs}}, \vec{k}, \nu_{\text{obs}}, \hat{n}) \approx \delta_{\text{HI}}(\vec{k}, z_{\text{em}})e^{-i\mu ks} + \mu^2 \delta(\vec{k}, z_{\text{em}})e^{-i\mu ks} + \mathcal{C}_{\delta_{\text{HI}}\delta}(\vec{k}, z_{\text{em}}, \hat{n})e^{-i\mu ks}, \quad (5)$$

where the cross-term is  $\mathcal{C}_{\delta_{\text{HI}}\delta}(\vec{k}, z_{\text{em}}, \hat{n}) \equiv \int \frac{d^3\vec{k}'}{(2\pi)^3} \delta_{\text{HI}}(\vec{k} - \vec{k}')\delta(\vec{k}', \hat{n})^2$ . Here  $\mu \equiv \hat{k} \cdot \hat{n}$ . The free-streaming projection of plane waves is manifest in Eq. (5), and both terms on its second line due to the RSD carry intrinsic angular dependence. Before and during the early phase of reionization, the convolution above is a second-order term so that the azimuthal symmetry around  $\vec{k}$  is preserved (Barkana & Loeb 2005; McQuinn et al. 2006). However, once  $\delta_{\text{HI}} \sim 1$ , the convolution term between the patchy H I field and the RSD may not be negligible even if the velocity field is still linear, breaking the azimuthal symmetry.

We will leave the investigation of the convolution term to a future work and drop it in this paper. This assumption is valid at large scales where  $\delta_{\text{HI}} < 1$  still holds. Under this assumption,  $\Theta(\eta_{\text{obs}}, \vec{k}, \nu_{\text{obs}}, \hat{n}) = \Theta(\eta_{\text{obs}}, \vec{k}, \nu_{\text{obs}}, \mu)$ , i.e. its dependence on the LoS is only through functions of  $\mu$ . Consequently, multipole moments of temperature anisotropies can be defined in the  $\hat{z} = \hat{k}$  frame (so that  $\mu = \cos\theta$ ):

$$\Theta_{\ell}(\eta_{\text{obs}}, \vec{k}, \nu_{\text{obs}}) \equiv \frac{1}{(-i)^{\ell}} \int_{-1}^1 \frac{d\mu}{2} \mathcal{P}_{\ell}(\mu) \Theta(\eta_{\text{obs}}, \vec{k}, \nu_{\text{obs}}, \mu) = \delta_{\text{HI}}(\vec{k}, z_{\text{em}}) j_{\ell}(ks) - \delta(\vec{k}, z_{\text{em}}) j_{\ell}''(ks), \quad (6)$$

where  $\mathcal{P}_{\ell}(\mu)$  is the Legendre polynomial,  $j_{\ell}(x)$  is the spherical Bessel function, and  $j_{\ell}''(x)$  is the second-

order derivative of  $j_{\ell}(x)$  with respect to its argument. The inverse transform is  $\Theta(\eta, \vec{k}, \nu, \mu) = \sum_{\ell} (2\ell + 1)(-i)^{\ell} \Theta_{\ell}(\eta, \vec{k}, \nu) \mathcal{P}_{\ell}(\mu)$ .

## 2.2. Linear polarization from electron scattering

Thomson scattering couples the intensity to the  $E$ -mode polarization, thereby generating the latter out of the unpolarized light. For scalar perturbations, the  $B$ -mode polarization is decoupled from the  $E$ -mode and vanishes under the azimuthal symmetry around  $\hat{k}$ . Analogous to the CMB, the transport of the 21 cm polarization signal follows the Boltzmann equations and its observed anisotropies can be calculated by the standard LoS integration formalism (Zaldarriaga & Seljak 1997; BL05). It exploits the multipole expansion (Eq. 6) in the  $\hat{z} = \hat{k}$  frame and yields the present-day observed (scalar) EE angular power spectrum, which is defined as  $C_{\ell}^{\text{EE}}(\eta_0, \nu_{\text{obs},0}) \equiv \langle |a_{E,\ell m}(\eta_0, \vec{x}_0, \nu_{\text{obs},0})|^2 \rangle$ , where  $a_{E,\ell m}$  are coefficients of the spherical harmonics decomposition. For a present-day Earth observer,  $\eta_{\text{obs}} = \eta_0$ ,  $\nu_{\text{obs}} = \nu_{\text{obs},0}$ ,  $z = z_{\text{em}}$ . Therefore, we have

$$C_{\ell}^{\text{EE}}(\eta_0, \nu_{\text{obs},0}) = 4\pi \left\langle \left| \int \frac{d^3\vec{k}}{(2\pi)^3} \Delta_{E\ell}(\eta_0, \vec{k}, \nu_{\text{obs},0}) \right|^2 \right\rangle. \quad (7)$$

In the expression above,  $\Delta_{E\ell}$  are multipole moments of  $E$ -mode polarization anisotropies in the  $\hat{z} = \hat{k}$  frame, and are derived in the standard LoS integration formalism. Here we write down its expression as follows:<sup>6</sup>

$$\Delta_{E\ell}(\eta_0, \vec{k}, \nu_{\text{obs},0}) \approx \frac{3}{4} \sqrt{\frac{(\ell+2)!}{(\ell-2)!}} \times \int_{\bar{\eta}_{z_{\text{em}}}}^{\bar{\eta}_0} g(\eta') \Pi(\eta', \vec{k}, \nu') \frac{j_{\ell}[ck(\bar{\eta}_0 - \eta')]}{[ck(\bar{\eta}_0 - \eta')]^2} d\eta', \quad (8)$$

where  $\nu' = \nu_{\text{obs},0}(1+z') \leq \nu_{21}$  is the frequency of 21 cm photons seen by an intervening free electron, for which the time of scattering is taken as the averaged cosmic time at  $z_{\text{cos}} = z'$ ,  $\eta' = \bar{\eta}_{z'}$ , and the source function  $\Pi(\eta', \vec{k}, \nu') = \Theta_2(\eta', \vec{k}, \nu') + \Delta_{P2}(\eta', \vec{k}, \nu') + \Delta_{P0}(\eta', \vec{k}, \nu')$ , where  $\Theta_2$  is the quadrupole moment of temperature fluctuations, and  $\Delta_{P\ell}$  and  $\Delta_{E\ell}$  are multipole moments of the total and  $E$ -mode polarization, respectively. The (global) visibility function is defined as  $g(\eta) \equiv -(\text{d}\tau/\text{d}\eta)e^{-\tau}$ , where  $\tau$  is the Thomson scattering optical depth,  $\tau(\eta) \equiv \int_{\eta}^{\eta_0} \bar{n}_e(\eta') \sigma_{\text{T}} c d\eta'$ ,  $\sigma_{\text{T}}$  is the Thomson scattering cross section.  $g(\eta)$  depends on the global

<sup>5</sup> Instead of taking the H I number density in the gas rest frame, we take the value measured in the perturbed FLRW frame. The difference is second-order in  $|v|/c$  and thus negligible.

<sup>6</sup> Eq. (8) is an approximate result in terms of the integration bounds applied to it. For those bounds, instead of applying the actual cosmic times,  $\eta_0$  and  $\eta_{\text{em}}$ , we use the ensemble-averaged values  $\bar{\eta}$  corresponding to cosmological redshifts  $z_{\text{cos}} = 0$  and  $z_{\text{cos}} = z_{\text{em}}$ , respectively, for the sake of brevity.

ionization history, illustrated in §3.2. In Eq. (8), the density of free electrons is approximated by the globally-averaged value,  $\bar{n}_e$ . However, in reality their distribution is patchy during the EoR and may cause secondary polarization (Hu 2000). This effect is worth future examinations but for now we neglect it as in BL05.

Given the low value of the electron scattering optical depth ( $\tau_{\text{es}} \sim 0.05$ ), it is reasonable to assume that most of the 21 cm photons do not scatter more than once by free electrons before they reach the observer. As a result, the relevant source function  $\Pi$  for 21 cm polarization (with the CMB part subtracted off) only has the contribution from the incident quadrupole,  $\Theta_2$ . (Note that this is not the case for the CMB in the tight

coupling limit). Also, under the current sensitivity of 21 cm experiments, the effect that the 21 cm temperature signal is suppressed by the factor  $\exp(-\tau_{\text{es}})$  due to Thomson scattering can be neglected so that  $\Theta(\vec{k}, \mu)$  remains at the free-streaming value (Eq. 5).

On the other hand,  $\Theta$  from Eq. (5) can be viewed as a decomposition according to the initial source fields,  $\delta_{\text{HI}}$  and  $\delta$ , which are statistically homogenous and isotropic. Each term has its own temperature transfer function:  $T_{\text{HI}}^{\text{T}}(\eta_{\text{obs}}, k, \nu_{\text{obs}}, \mu) = e^{-i\mu ks}$  and  $T_{\delta}^{\text{T}}(\eta_{\text{obs}}, k, \nu_{\text{obs}}, \mu) = \mu^2 e^{-i\mu ks}$ . Evidently, Eq. (6) means that multipole moments of these temperature transfer functions are  $T_{\text{HI},\ell}^{\text{T}}(\eta_{\text{obs}}, k, \nu_{\text{obs}}) = j_{\ell}[ck(\bar{\eta}_{z_{\text{obs}}} - \bar{\eta}_{z_{\text{em}}})]$  and  $T_{\delta,\ell}^{\text{T}}(\eta_{\text{obs}}, k, \nu_{\text{obs}}) = -j_{\ell}''[ck(\bar{\eta}_{z_{\text{obs}}} - \bar{\eta}_{z_{\text{em}}})]$ .

---

Thus, the present-day EE power spectrum can be explicitly written as

$$C_{\ell}^{\text{EE}}(\eta_0, \nu_{\text{obs},0}) = \frac{2}{\pi} \int k^2 dk \left[ P_{\text{HI}}(k, z_{\text{em}}) (\mathcal{T}_{\text{HI},\ell}^{\text{E}}(k))^2 + P_{\delta}(k, z_{\text{em}}) (\mathcal{T}_{\delta,\ell}^{\text{E}}(k))^2 + 2P_{\text{HI}\delta}(k, z_{\text{em}}) \mathcal{T}_{\text{HI},\ell}^{\text{E}}(k) \mathcal{T}_{\delta,\ell}^{\text{E}}(k) \right]. \quad (9)$$

Here the multipole moments of the  $E$ -mode polarization transfer functions in the integrand of the RHS of Eq. (9), as well as those temperature transfer functions in the integrand of the RHS of Eq. (11–12) below, are all implicitly evaluated at  $(\eta_0, \nu_{\text{obs},0})$ ,

$$\mathcal{T}_{\text{HI},\ell}^{\text{E}}(\eta_0, k, \nu_{\text{obs},0}) \equiv \frac{3}{4} \sqrt{\frac{(\ell+2)!}{(\ell-2)!}} \int_{\bar{\eta}_{z_{\text{em}}}}^{\bar{\eta}_0} g(\eta') j_2[ck(\eta' - \bar{\eta}_{z_{\text{em}}})] \frac{j_{\ell}[ck(\bar{\eta}_0 - \eta')]}{[ck(\bar{\eta}_0 - \eta')]^2} d\eta', \quad (10a)$$

$$\mathcal{T}_{\delta,\ell}^{\text{E}}(\eta_0, k, \nu_{\text{obs},0}) \equiv -\frac{3}{4} \sqrt{\frac{(\ell+2)!}{(\ell-2)!}} \int_{\bar{\eta}_{z_{\text{em}}}}^{\bar{\eta}_0} g(\eta') j_2''[ck(\eta' - \bar{\eta}_{z_{\text{em}}})] \frac{j_{\ell}[ck(\bar{\eta}_0 - \eta')]}{[ck(\bar{\eta}_0 - \eta')]^2} d\eta'. \quad (10b)$$

Here  $P_{\text{HI}}$  and  $P_{\delta}$  are the (equal-time) H I density and matter power spectra, respectively, and  $P_{\text{HI}\delta}$  is the cross-power spectrum between the H I and the matter field. They are defined as  $\langle \delta_{\text{HI}}^*(\vec{k}) \delta_{\text{HI}}(\vec{k}') \rangle \equiv (2\pi)^3 P_{\text{HI}}(k) \delta_{\text{D}}^{(3)}(\vec{k} - \vec{k}')$ ,  $\langle \delta^*(\vec{k}) \delta(\vec{k}') \rangle \equiv (2\pi)^3 P_{\delta}(k) \delta_{\text{D}}^{(3)}(\vec{k} - \vec{k}')$ , and  $\langle \delta_{\text{HI}}^*(\vec{k}) \delta(\vec{k}') \rangle \equiv (2\pi)^3 P_{\text{HI}\delta}(k) \delta_{\text{D}}^{(3)}(\vec{k} - \vec{k}')$ . Finally, to obtain dimensional quantities, the extra coefficient of  $[T_0(z_{\text{em}}) \bar{x}_{\text{HI},\text{m}}(z_{\text{em}})]^2$  should be multiplied to the result of the dimensionless angular power spectrum.

Similarly, the temperature power spectrum observed today,  $C_{\ell}^{\text{TT}} = 4\pi \left\langle \left| \int d^3\vec{k} \Theta_{\ell}(\eta_0, k, \nu_{\text{obs},0}) / (2\pi)^3 \right|^2 \right\rangle$ , is given by

$$C_{\ell}^{\text{TT}}(\eta_0, \nu_{\text{obs},0}) = \frac{2}{\pi} \int k^2 dk \left[ P_{\text{HI}}(k, z_{\text{em}}) (T_{\text{HI},\ell}^{\text{T}}(k))^2 + P_{\delta}(k, z_{\text{em}}) (T_{\delta,\ell}^{\text{T}}(k))^2 + 2P_{\text{HI}\delta}(k, z_{\text{em}}) T_{\text{HI},\ell}^{\text{T}}(k) T_{\delta,\ell}^{\text{T}}(k) \right]. \quad (11)$$

The cross-power spectrum between the temperature and the  $E$ -mode polarization is

$$C_{\ell}^{\text{TE}}(\eta_0, \nu_{\text{obs},0}) = \frac{2}{\pi} \int k^2 dk \left\{ P_{\text{HI}}(k, z_{\text{em}}) T_{\text{HI},\ell}^{\text{T}}(k) \mathcal{T}_{\text{HI},\ell}^{\text{E}}(k) + P_{\delta}(k, z_{\text{em}}) T_{\delta,\ell}^{\text{T}}(k) \mathcal{T}_{\delta,\ell}^{\text{E}}(k) + P_{\text{HI}\delta}(k, z_{\text{em}}) [T_{\text{HI},\ell}^{\text{T}}(k) \mathcal{T}_{\delta,\ell}^{\text{E}}(k) + T_{\delta,\ell}^{\text{T}}(k) \mathcal{T}_{\text{HI},\ell}^{\text{E}}(k)] \right\}. \quad (12)$$

---

Eqs. (9) and (12) describe the signals that we seek in this paper. Compared with BL05, our expressions take advantage of a more complete decomposition of the signal, and, in addition, includes contributions from cross-

---

correlations between the initial source fields. The case in which 21 cm brightness temperature fluctuations are sourced by multiple cosmological fields in a more general context is formulated in Appendix B.



### 3. REIONIZATION MODEL

The dominant source for the EoR signal is the ionization field, or equivalently, the neutral fraction field,  $\delta x_{\text{HI}} \equiv x_{\text{HI}}/\bar{x}_{\text{HI}} - 1$  ( $\bar{x}_{\text{HI}}$  is the *volume-weighted* average neutral fraction). It is patchy and nonlinear during the bulk of cosmic reionization. So far, the most prevalent analytical model of reionization has been the bubble model (e.g., [Gruzinov & Hu 1998](#); [Knox et al. 1998](#)). BL05 employed a simple bubble model to estimate the neutral fraction power spectrum, which assumes that H II regions are randomly-distributed, fully-ionized spheres. However, more sophisticated bubble model has been introduced, based on the excursion set formalism ([Furlanetto et al. 2004b](#)), which relates the emissivity of ionizing sources to the underlying matter distribution. Based upon this treatment, efficient seminumerical algorithms have been developed to generate the realizations of ionization fields without the radiative transfer computation (e.g., [Santos et al. 2010](#); [Mesinger et al. 2011](#)), which also allows for partially-ionized H II regions. We will employ the seminumerical approach to estimate the ionization power spectra since it can model the effect of patchy reionization more realistically. Note that cosmological radiative transfer simulations of reionization (e.g., [Iliev et al. 2014](#); [Aubert et al. 2015](#)) can provide even more accurate modeling than the seminumerical method, but their difference is mainly in the accuracy and should not affect the conclusions herein.

In §3.1 we briefly review the toy model in BL05 for the sake of comparison. In §3.2 we present our seminumerical simulations which yield ionization histories consistent with all current constraints. The resulted H I density fields will serve as the initial conditions for calculating the 21 cm polarization signal.

#### 3.1. Analytical model in BL05

In BL05, the dimensionless brightness temperature is evaluated using the third line of Eq. (2), such that

$$\psi \equiv x_{\text{HI}} [1 + \Delta] = x_{\text{HI}} + \bar{x}_{\text{HI}} [\Delta + \delta x_{\text{HI}} \Delta], \quad (13)$$

where  $\Delta \equiv \delta - (1/\mathcal{H})(\partial v_{\parallel}/\partial r)$ . The nonlinear cross term  $\delta x_{\text{HI}} \Delta$  is not negligible when fluctuations in the ionization field is significant ( $\delta x_{\text{HI}} \sim 1$ ). As discussed before, it breaks the azimuthal symmetry in Fourier space. BL05 ignored this nonlinear term anyway (so that  $\psi \approx x_{\text{HI}} + \bar{x}_{\text{HI}} \Delta$ ) and calculated the temperature multipole  $\Theta_{\ell}(\vec{k})$  as follows:

$$\bar{x}_{\text{HI},\text{m}}(z_{\text{em}}) \Theta_{\ell}(\eta_{\text{obs}}, \vec{k}, \nu_{\text{obs}}) \approx \bar{x}_{\text{HI}}(z_{\text{em}}) \left[ \delta x_{\text{HI}}(\bar{\eta}_{z_{\text{em}}}, \vec{k}) j_{\ell}(ks) + \delta(\bar{\eta}_{z_{\text{em}}}, \vec{k}) \left( j_{\ell}(ks) - j_{\ell}''(ks) \right) \right]. \quad (14)$$

Following the standard procedure, the formulae of 21 cm polarization angular power spectra in BL05 (their Eqs. 13 and 25) can be rewritten using *our* notation<sup>7</sup> as

$$C_{\ell}^{\text{EE}} = \frac{2}{\pi} \int k^2 dk \left\{ [\bar{x}_{\text{HI}}^{-2} P_x(k) + P_{\delta}(k)] (\mathcal{T}_{\text{HI},\ell}^{\text{E}}(k))^2 + P_{\delta}(k) (\mathcal{T}_{\delta,\ell}^{\text{E}}(k))^2 + 2 P_{\delta}(k) \mathcal{T}_{\text{HI},\ell}^{\text{E}}(k) \mathcal{T}_{\delta,\ell}^{\text{E}}(k) \right\}, \quad (15)$$

$$C_{\ell}^{\text{TE}} = \frac{2}{\pi} \int k^2 dk \left\{ [\bar{x}_{\text{HI}}^{-2} P_x(k) + P_{\delta}(k)] T_{\text{HI},\ell}^{\text{T}}(k) \mathcal{T}_{\text{HI},\ell}^{\text{E}}(k) + P_{\delta}(k) T_{\delta,\ell}^{\text{T}}(k) \mathcal{T}_{\delta,\ell}^{\text{E}}(k) + P_{\delta}(k) [T_{\text{HI},\ell}^{\text{T}}(k) \mathcal{T}_{\delta,\ell}^{\text{E}}(k) + T_{\delta,\ell}^{\text{T}}(k) \mathcal{T}_{\text{HI},\ell}^{\text{E}}(k)] \right\}, \quad (16)$$

where all the transfer functions are evaluated at  $(\eta_0, \nu_{\text{obs},0})$ , all the power spectra and  $\bar{x}_{\text{HI}}$  are evaluated at  $z_{\text{em}}$ , and the dimensional results should be obtained by multiplying the extra factor of  $[T_0(z_{\text{em}}) \bar{x}_{\text{HI},\text{m}}(z_{\text{em}})]^2$ .

Comparing Eqs. (15 and 16) with Eqs. (9 and 12), it is realized that the approximations made in BL05 are  $P_{\text{HI}}(k) \approx \bar{x}_{\text{HI}}^{-2} P_x(k) + P_{\delta}(k)$  and  $P_{\text{HI}\delta}(k) \approx P_{\delta}(k)$ . Since  $\delta_{\text{HI}} = \delta x_{\text{HI}} + \delta + \delta x_{\text{HI}} \delta$ , we have  $P_{\text{HI}}(k) = \bar{x}_{\text{HI}}^{-2} P_x(k) + P_{\delta}(k) + 2\bar{x}_{\text{HI}}^{-1} P_{x_{\text{HI}}\delta} + (\text{higher-order cross terms})$ , and  $P_{\text{HI}\delta}(k) = P_{\delta}(k) + \bar{x}_{\text{HI}}^{-1} P_{x_{\text{HI}}\delta} + (\text{higher-order cross terms})$ . Therefore, not only did BL05 ignore the higher-order cross terms due to  $\delta x_{\text{HI}} \delta$ , but also it ignored the leading-order cross term  $P_{x_{\text{HI}}\delta}$  which is important and non-negligible as we will show in §3.2 (see Figure 2). In comparison, our formalism is expanded on the H I density fluctuations, which automatically corrects for both issues.

In BL05, the only target of the EoR modeling is the ionization power spectrum,  $P_x(k)$ , i.e. the power spectrum of the *neutral fraction* field  $x_{\text{HI}}$ . Its modeling of  $P_x(k)$  was based on an analytical argument about Poisson-randomly-distributed bubbles (BL05; [De & Tashiro 2014](#)), only applicable near the end of the EoR. Reionization is assumed to be sudden at  $z_{\text{re}}$ . Their result is

$$P_x(k) = \frac{4\pi R^3}{3} e^{-k^2 R^2}, \quad (17)$$

where  $R$  is the characteristic radius of bubbles at that time,  $R \propto (1+z_{\text{re}})^{-3/2}$  ([Wyithe & Loeb 2004](#)). However, this power spectrum cannot be realistic since it does not vanish when reionization ends ( $\bar{x}_{\text{HI}} \rightarrow 0$ ). Therefore, in this paper, we will not compare our results with Eq. (17).

A more realistic analytical model was given by [Zaldarriaga et al. \(2004\)](#) which also assumes randomly-distributed, single-size bubbles, but is not restricted to

<sup>7</sup> Note that in BL05, the multipole moments of the transfer functions due to the RSD,  $T_{\delta,\ell}^{\text{T}}$  and  $\mathcal{T}_{\delta,\ell}^{\text{E}}$ , take different forms from ours. This can be understood by comparing Eq. (6) with Eq. (14).

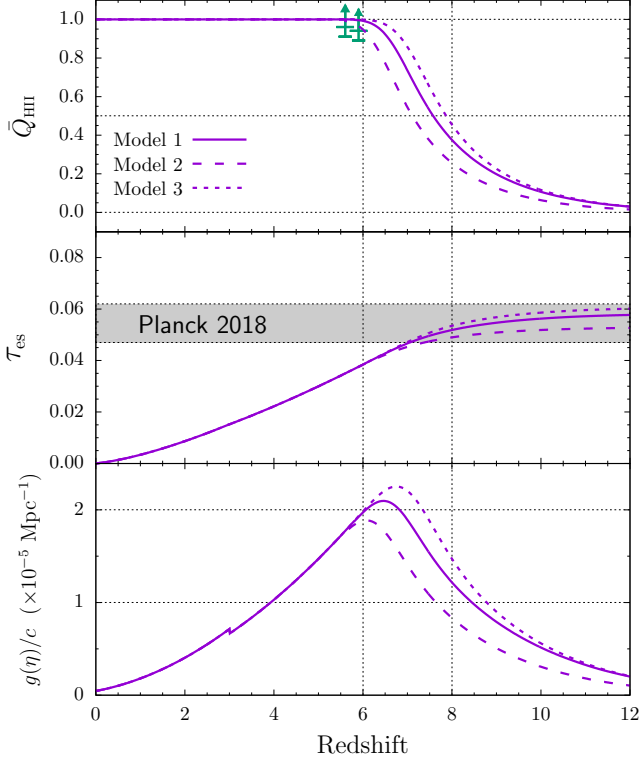


**Figure 1.** Reionization histories generated by the seminumerical simulations of reionization with EoR model parameters ( $\zeta, T_{\text{vir}}, R_{\text{mfp}}$ ) in Table 1 (solid/dashed/dotted curves for Model 1/2/3). Shown are the H II volume filling fraction  $\bar{Q}_{\text{HII}}$  (top), the CMB Thomson scattering optical depth  $\tau_{\text{es}}$  (middle), and the visibility function normalized by  $c$ ,  $g(\eta)/c$  (bottom), as a function of redshift. These reionization histories are all consistent with  $1\sigma$  constraints from the fraction of “dark” pixels in the Ly $\alpha$  and Ly $\beta$  forests (McGreer et al. 2015, arrows in the top panel) and the global  $\tau_{\text{es}}$  inferred by the CMB (Planck Collaboration et al. 2020, the shaded area in the middle panel). In the bottom panel, the discontinuity at  $z = 3$  is due to He II reionization.

the end of the EoR and satisfies the constraint that  $P_x(k) \rightarrow 0$  when reionization finishes. According to their model,

$$P_x(k) = (\sqrt{2\pi}R)^3 (\bar{x}_{\text{HI}} - \bar{x}_{\text{HI}}^2) e^{-k^2 R^2/2}. \quad (18)$$

In this paper, we will improve upon the analytical modeling (Eq. 18) by the realistic modeling of H I density power spectrum using seminumerical reionization simulations, and compare their results in the next sections.

### 3.2. Seminumerical reionization simulations

The density fields and ionization fields are generated from cosmological seminumerical simulations of reionization using the 21cmFAST code<sup>8</sup> (Mesinger et al. 2011),

<sup>8</sup> <https://github.com/andreimesinger/21cmFAST>

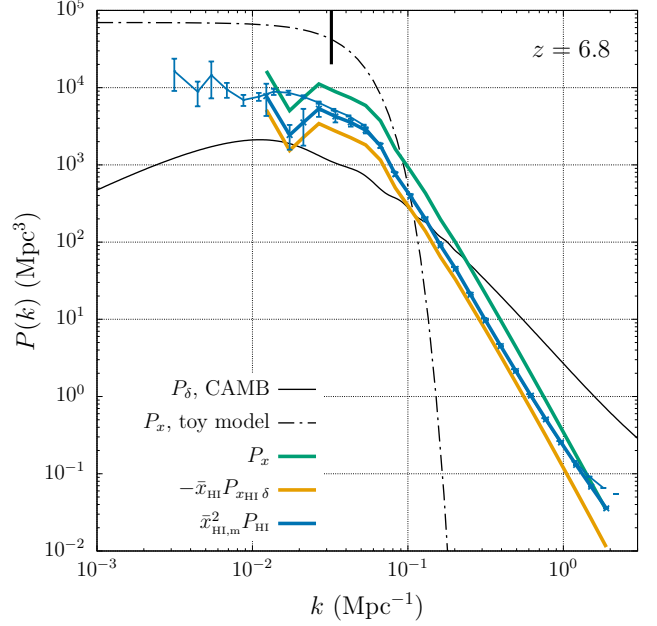


**Figure 2.** Power spectra of various sources at  $z = 6.8$  (corresponding to  $\bar{Q}_{\text{HII}} \approx 0.82$  in Model 1). Shown are the neutral fraction power spectrum  $P_x(k)$  (green solid line), the H I density power spectrum  $P_{\text{HI}}(k)$  (blue solid line), and the neutral fraction-density cross-power spectrum  $P_{x_{\text{HI}} \delta}(k)$  (yellow solid line), with the latter two power spectra being weighted by relevant factors. These power spectra are calculated from the seminumerical simulations of reionization: the thick lines are from the small-box simulation (512 cMpc per side), and the blue thin line is the additional result of the H I density power spectrum from the large-box one (2000 cMpc per side). The error bars on  $P_{\text{HI}}$  represent the sample variances corresponding to each simulation volume. For the purpose of comparison, we also show the matter power spectrum produced by CAMB (black solid line), and the neutral fraction power spectrum  $P_x(k)$  from the toy model using Eq. (18) (dot-dashed line) with the characteristic bubble radius in this toy model indicated by the black thick vertical line.

**Table 1.** EoR model parameters

Model	$\zeta$	$T_{\text{vir}}$ [K]	$R_{\text{mfp}}$ [cMpc]
1	30	$6 \times 10^4$	40
2	35	$1 \times 10^5$	40
3	40	$7 \times 10^4$	35

with two choices of comoving boxes: the large box with 2000 cMpc per side and the small box with 512 cMpc per side. For the large (small) box, initial conditions are created on a  $4000^3$  ( $4096^3$ ) grid, and smoothed down to a  $1000^3$  ( $1024^3$ ) grid for the reionization simulation. We

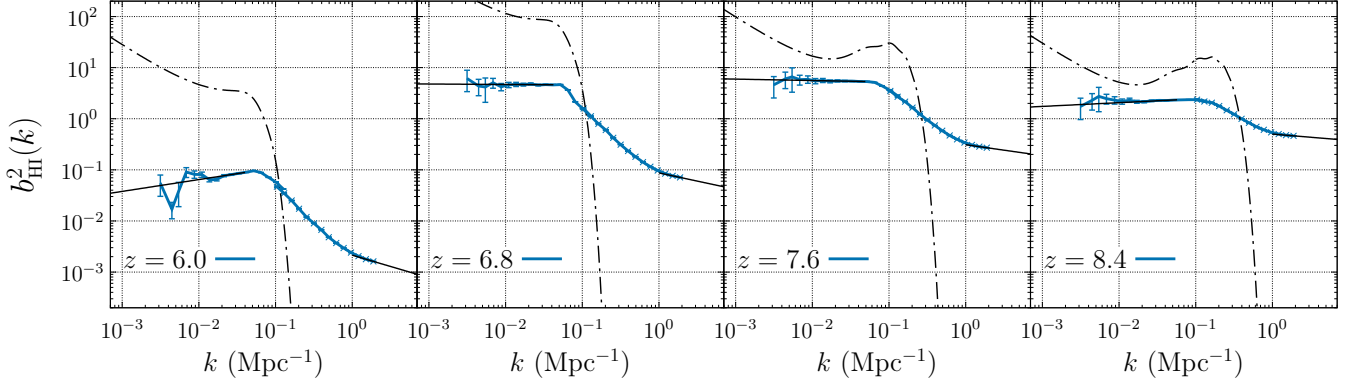


**Figure 3.** The H I bias at different redshifts during the EoR. Shown are the results from seminumerical reionization simulations for Model 1 (blue solid lines with error bars representing the sample variance), and those from the toy model (Eq. 18, dot-dashed lines). We extrapolate the bias from simulation with power-law fits (black solid lines) at both high and low ends of the  $k$  range beyond the simulation coverage.

output data at desired redshifts during the post-heating phase of the EoR, ranging from  $z = 10$  to  $z = 5.6$ .

The simulations are based on three fundamental parameters in the EoR modeling:  $\zeta$  (ionization efficiency),  $T_{\text{vir}}$  (the minimum virial temperature of halos that host ionizing sources), and  $R_{\text{mfp}}$  (the maximum mean free path of ionizing photons). Detailed astrophysical interpretations of these parameters and how the global ionization history depends on them can be found in Greig & Mesinger (2017). While simplistic, this model has been compared with full numerical simulations to show that it can reproduce the realistic 3D maps of the EoR in terms of both morphology and statistics within reasonable accuracy (Majumdar et al. 2014).

For both the large and small boxes, we apply multiple sets of EoR parameters, labeled as “Model 1-3” in Table 1.<sup>9</sup> They generate different global ionization histories, and thus different electron scattering optical depths and visibility functions (defined in §2.2). Figure 1 shows their evolution, compared with current model-independent observational constraints from the fraction of “dark” pixels in the Ly $\alpha$  and Ly $\beta$  forests and the global Thomson optical depth inferred by the CMB.  $\bar{Q}_{\text{HII}} \equiv 1 - \bar{x}_{\text{HI}}$  defines the H II volume filling fraction (a.k.a. the global ionized fraction). For each model in Table 1, we have verified that the global evolutions from the two box sizes are consistent. The bottom panel of Figure 1 shows that the visibility function, while reaching its maximum near the end of the EoR, demonstrates a broad width over redshift, in contrast to the sharply-peaked  $g(\eta)$  at recombination with respect to the CMB.

Therefore, the LoS integration in Eqs. (10a–10b) is more time-consuming than in the CMB case.

We illustrate in Figure 2 the (equal-time) power spectrum of the H I density field,  $P_{\text{HI}}(k)$ , and that of the neutral fraction field,  $P_x(k)$ , obtained from simulation data. The matter power spectrum is calculated using the CAMB package<sup>10</sup>. The power spectra –  $P_{\text{HI}}(k)$ ,  $P_x(k)$ , and the cross-power  $P_{x_{\text{HI}}\delta}(k)$  – have similar shapes on all scales of interest, which indicates that the neutral fraction fluctuations dominate over the density fluctuations. For the purpose of a fair comparison between the toy model in BL05 and the seminumerical simulations, we set the characteristic bubble radius at the end of reionization in the toy model to be the photon horizon in the simulation, and take into account its growth during the EoR.  $P_x(k)$  from the toy model in Eq. (18) shows an exponential cutoff on small scales, but the simulation result shows a slower decrease. On scales larger than the characteristic bubble radius, however, the analytical model overestimates the power spectrum by nearly one order of magnitude. The reason is that the toy model assumes fully ionized bubbles, yet realistic H II regions can have internal structures, thereby leading to less fluctuation amplitudes for the fixed global ionized fraction.

Moreover, Figure 2 clearly shows that the neutral fraction and the matter overdensity field are anti-correlated, as a result of the inside-out reionization scenario, and their cross-power spectrum,  $P_{x_{\text{HI}}\delta}(k)$ , is a non-negligible contribution to the H I density power spectrum.

In order to calculate the temperature and polarization anisotropy (Eqs. 9, 11 and 12), we need  $P_{\text{HI}}(k)$  on all scales. For the  $k$  range covered by simulations, we stitch together the results from the large and small

<sup>9</sup> In this paper, we assume a  $\Lambda$ CDM cosmology with  $\Omega_m = 0.32$ ,  $\Omega_b = 0.05$ ,  $h = 0.67$ ,  $n_s = 0.97$  and  $\sigma_8 = 0.81$ , in consistent with the Planck 2018 results (Planck Collaboration et al. 2020).

<sup>10</sup> <https://camb.info/>



boxes and discard data from  $k > 2 \text{ Mpc}^{-1}$ , to avoid the alias effect. For scales beyond either side of the simulation coverage, we assume a power-law H I bias,  $b_{\text{HI}}^2(k) \equiv P_{\text{HI}}(k)/P_{\delta}(k) \propto k^n$ . The overall result of  $b_{\text{HI}}^2(k)$  is shown in Figure 3. Whereas the H I distribution on scales below the characteristic bubble size can contain richer information than encoded by only the power spectrum, we expect the distribution of H I gas to follow the underlying total matter on large scales. Figure 3 confirms that the bias is nearly linear on super bubble scales throughout the EoR.<sup>11</sup> The behavior of the H I bias from the toy model is very different, because  $P_x(k)$  approaches constant as  $k \rightarrow 0$  in Eq. (18). As we will see in the §4 below, the shape of the large-scale H I bias (or power spectrum) leads to distinguishable patterns in the 21 cm polarization signal.

#### 4. RESULTS

We discuss the patterns and physical implications of the 21 cm TT, TE and EE power spectra with a fiducial model in §4.1, and focus on the evolution of  $C_{\ell}^{\text{TE}}$  and  $C_{\ell}^{\text{EE}}$  during the EoR and present their dependence on the global ionization history in §4.2.

##### 4.1. Generic feature of angular power spectra

In Figure 4, we illustrate the 21 cm temperature and polarization angular power spectrum in Model 1, at  $z_{\text{em}} = 6.8$  ( $\bar{Q}_{\text{HII}} \approx 0.82$ ). It shows that the temperature-polarization cross-power spectrum,  $C_{\ell}^{\text{TE}}$ , is about four orders of magnitude smaller than the temperature power spectrum  $C_{\ell}^{\text{TT}}$ , and the polarization power spectrum  $C_{\ell}^{\text{EE}}$  is three orders of magnitude even smaller than  $C_{\ell}^{\text{TE}}$ . This will make the detection of 21 cm polarization signal very difficult, as we will see in §5. Regarding the comparison with the toy model, on the other hand, it shows that the toy model always underestimates the polarization (EE and TE) powers on small scales but overestimates them on large scales.

For the temperature power spectrum, it turns out to be like a white noise on large scales, i.e.  $C_{\ell}^{\text{TT}} = \text{constant}$  for small  $\ell$  (Lewis & Challinor 2007). This is because for small  $\ell$  it is dominated by the contributions from the  $k$ -modes of small scales ( $ks > \ell$ ) rather than those of comparable scales. This is illustrated in Figure 5. While the temperature transfer function  $T_{\text{HI},\ell}^{\text{T}}(k)$  peaks near  $k_* \simeq \ell/s$ , the H I power spectrum peaks at much smaller scale. As a result, it turns out that the integrand

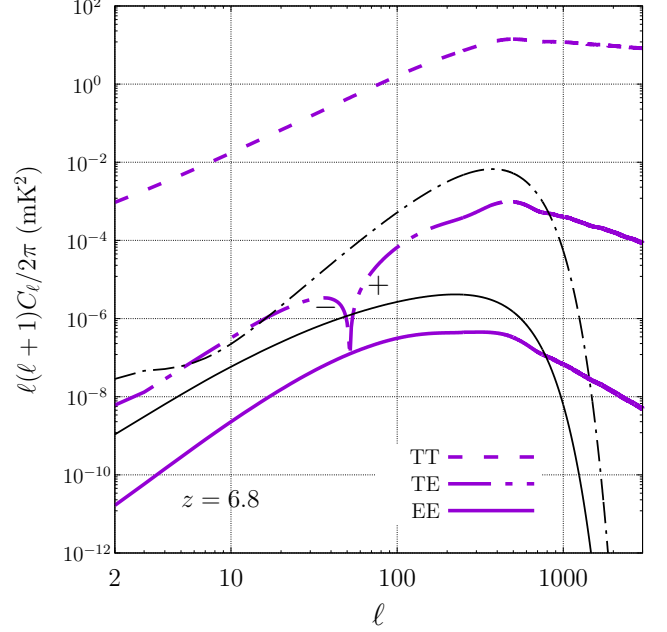


**Figure 4.** Angular power spectra of the 21 cm temperature (TT, dashed),  $E$ -mode polarization (EE, solid) and the temperature-polarization cross-correlation (TE, dot-dashed) at  $z_{\text{em}} = 6.8$ . Shown are the results from the Model 1 of seminumerical simulation (thick purple lines), and from the toy model (Eq. 18, thin black lines). The TE power spectrum from simulation is plotted with its absolute value, with the minus/plus sign marking the negative/positive part on the left/right-hand side of a sharp zero-crossing.

of  $C_{\ell}^{\text{TT}}$  (see Eq. 11) peaks at a scale much smaller than  $k_*$  for small  $\ell$  (see the bottom panel of Figure 5). Given the shape of  $\Delta_{\text{HI}}^2(k)$ , only for large enough  $\ell$  ( $\ell \gtrsim 100$ ) does the majority of contributions to the  $C_{\ell}^{\text{TT}}$  integration come from the modes of comparable scales  $k_*$ .

However, this is not the case for the temperature-polarization cross-power spectrum,  $C_{\ell}^{\text{TE}}$ , which involves the transfer function of the  $E$ -mode polarization. Figure 6 shows that in  $C_{\ell}^{\text{TE}}$  the integration in Eq. (12) is indeed dominated by the modes near the characteristic scale  $k_* = \ell/s$ , for all  $\ell$ . Furthermore, since  $T_{\text{HI},\ell}^{\text{T}} \mathcal{T}_{\text{HI},\ell}^{\text{E}}$  can be negative, as shown in Figure 6, the integrand of  $C_{\ell}^{\text{TE}}$  has negative parts, and those negative parts become more important as  $\ell$  is smaller. As a result, the integration over Fourier modes can result in negative values when  $\ell$  is small. This is why  $C_{\ell}^{\text{TE}}$  from simulation results turns from positive to negative at  $\ell \lesssim 50$ , as we find in Figure 4. However, we also find in Figure 4 that  $C_{\ell}^{\text{TE}}$  from the toy model is always positive. This is because the toy model significantly overestimates the H I power spectrum at small  $k$  where  $T_{\text{HI},\ell}^{\text{T}}$  and  $\mathcal{T}_{\text{HI},\ell}^{\text{E}}$  are mostly positive, thereby enhancing the values of the integrand toward small  $k$ . This comparison between simu-

<sup>11</sup> The caveat is a scale-dependent bias at the end of EoR  $z = 6.0$  as shown in the left panel of Figure 3, but this is likely due to numerical artifact which arises because the seminumerical reionization simulation based on the excursion set model fails at that time.

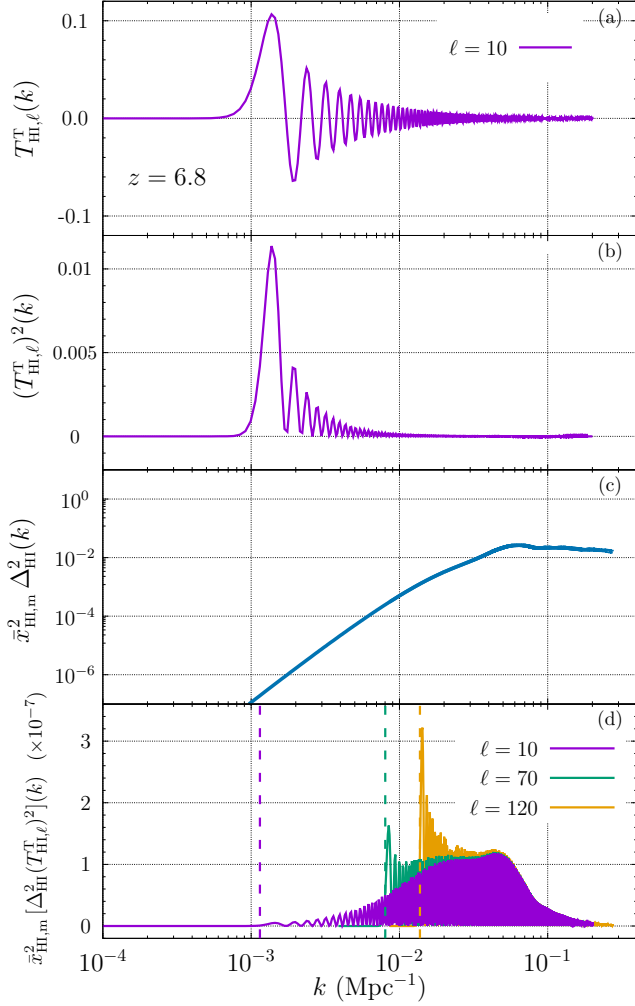


**Figure 5.** Contributions to the  $C_\ell^{\text{TT}}$  integration at  $z_{\text{em}} = 6.8$  in Model 1. (a) temperature transfer function of H I density fluctuations,  $T_{\text{HI},\ell}^{\text{T}}(k)$  with  $\ell = 10$ . (b)  $(T_{\text{HI},\ell}^{\text{T}}(k))^2$  with  $\ell = 10$ . (c) the dimensionless H I power spectrum,  $\Delta_{\text{HI}}^2(k) \equiv k^3 P_{\text{HI}}(k)/2\pi^2$ , weighted with relevant factor, from simulation. (Note that the power spectra at both high and low ends of the  $k$  range beyond the simulation coverage is obtained by extrapolating the H I bias from simulation with power-law fits.) (d) the leading term in the integrand of  $C_\ell^{\text{TT}}$  in Eq. (11),  $\bar{x}_{\text{HI},\text{m}}^2 \Delta_{\text{HI}}^2 (T_{\text{HI},\ell}^{\text{T}})^2$  (i.e. product of the quantities in (b) and (c)), as a function of wavenumber  $k$ , at various angular scales,  $\ell = 10/70/120$  (purple/green/yellow). The characteristic scale  $k_* = \ell/s$  at  $z_{\text{em}} = 6.8$  is indicated by the vertical lines for  $\ell$  of the same color.

lation and toy model results implies that the sign of  $C_\ell^{\text{TE}}$  is sensitive to the linear H I bias at large scales, and the shape of  $C_\ell^{\text{TE}}$  may be used to probe the value of linear H I bias during the EoR at the super-bubble scales (scales larger than the typical bubble size but smaller than the Hubble radius).

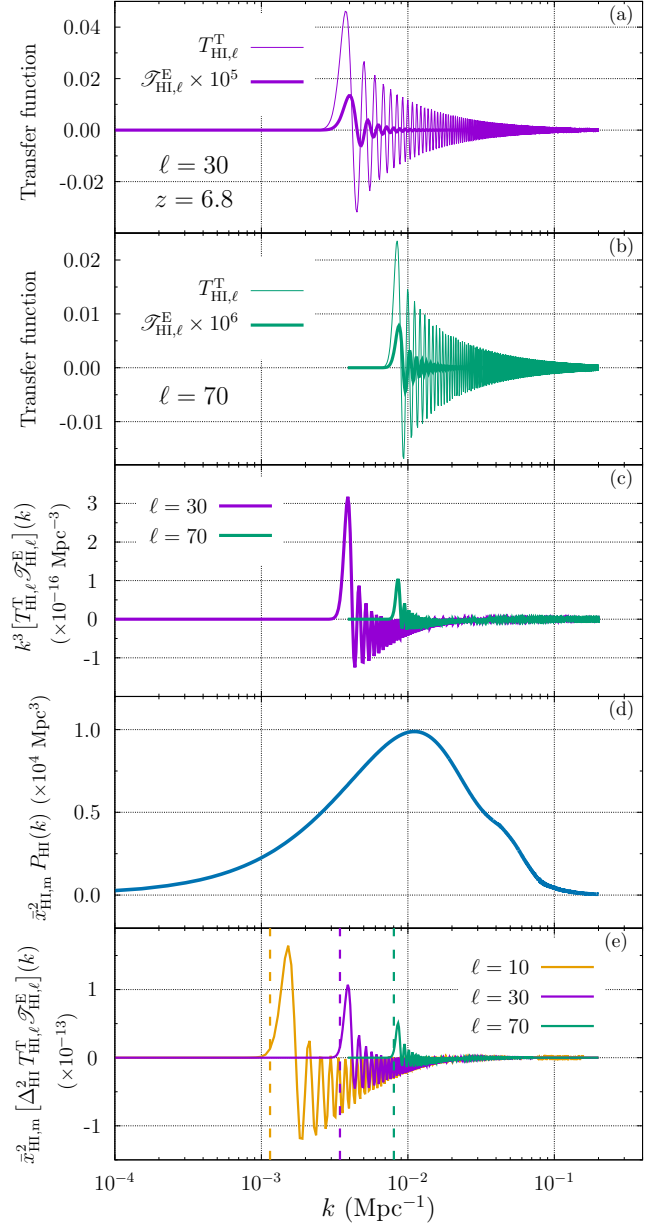


**Figure 6.** Contributions to the  $C_\ell^{\text{TE}}$  integration at  $z_{\text{em}} = 6.8$  in Model 1. (a) temperature and polarization transfer functions of H I density fluctuations  $T_{\text{HI},\ell}^{\text{T}}(k)$  (thin) and  $\mathcal{S}_{\text{HI},\ell}^{\text{E}}(k)$  (thick) at  $\ell = 30$ . (b) same as in (a) but for  $\ell = 70$ . (c)  $k^3 T_{\text{HI},\ell}^{\text{T}} \mathcal{S}_{\text{HI},\ell}^{\text{E}}$  for  $\ell = 30/70$  (purple/green). (d) H I density power spectrum  $P_{\text{HI}}(k)$ , weighted with relevant factor, from simulation. (e) the leading term in the integrand of  $C_\ell^{\text{TE}}$  in Eq. (12),  $\bar{x}_{\text{HI},\text{m}}^2 \Delta_{\text{HI}}^2 T_{\text{HI},\ell}^{\text{T}} \mathcal{S}_{\text{HI},\ell}^{\text{E}}$  as a function of wavenumber  $k$ , at various angular scales,  $\ell = 10/30/70$  (yellow/purple/green). The characteristic scale  $k_* = \ell/s$  at  $z_{\text{em}} = 6.8$  is indicated by the vertical lines for  $\ell$  of the same color.

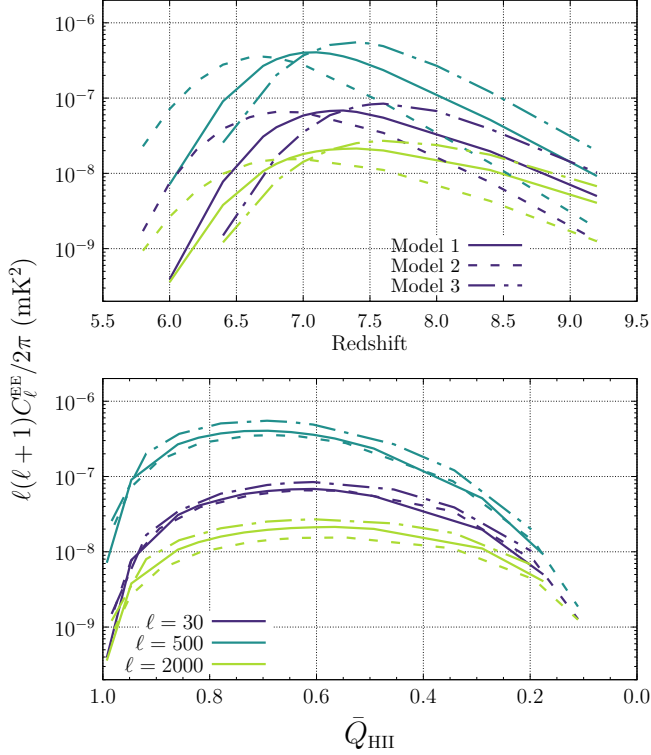


**Figure 7.** Evolution of the EE power spectrum  $C_\ell^{\text{EE}}$  at different angular scales  $\ell = 30/500/2000$  (purple/dark green/light green) during the EoR for different Model 1/2/3 (solid/dashed/dot-dashed line). (Top)  $C_\ell^{\text{EE}}$  as a function of redshift. (Bottom)  $C_\ell^{\text{EE}}$  as a function of the global H II volume filling fraction.

The EE power spectrum  $C_\ell^{\text{EE}}$  in Figure 4 shows a plateau on the intermediate angular scales and turns over at the scale of the typical bubble size ( $\ell \sim s/R$ ). The bump feature is caused by the turnover in the H I density power spectrum (see Figure 2). This feature due to the morphological structure of cosmic H II regions during the EoR is also reflected in  $C_\ell^{\text{TE}}$  at the angular scale of bubble size ( $\ell \sim s/R$ ), as shown in Figure 4.

#### 4.2. Evolution and model-dependence

We plot the evolution of EE and TE power spectra, in Figures 7 and 8 respectively, at three representative angular scales corresponding to linear scales ( $\ell = 30$ ), the plateau (or the peak,  $\ell = 500$ ), and sub-bubble scales ( $\ell = 2000$ ). For both  $C_\ell^{\text{EE}}$  and  $C_\ell^{\text{TE}}$ , all curves exhibit a similar trend in the evolution of the amplitude of the signal: as reionization proceeds, the signal first rises to its peak and then gradually drops to almost zero when the IGM becomes fully ionized. The location of the peak is dependent on  $\ell$  but insensitive to the ionization history, within a broad range  $\bar{Q}_{\text{HII}} \sim 0.50 - 0.70$ . Furthermore, Figure 9 shows the evolution of the ratio  $C_\ell^{\text{EE}}/C_{\ell,\text{max}}^{\text{EE}}$

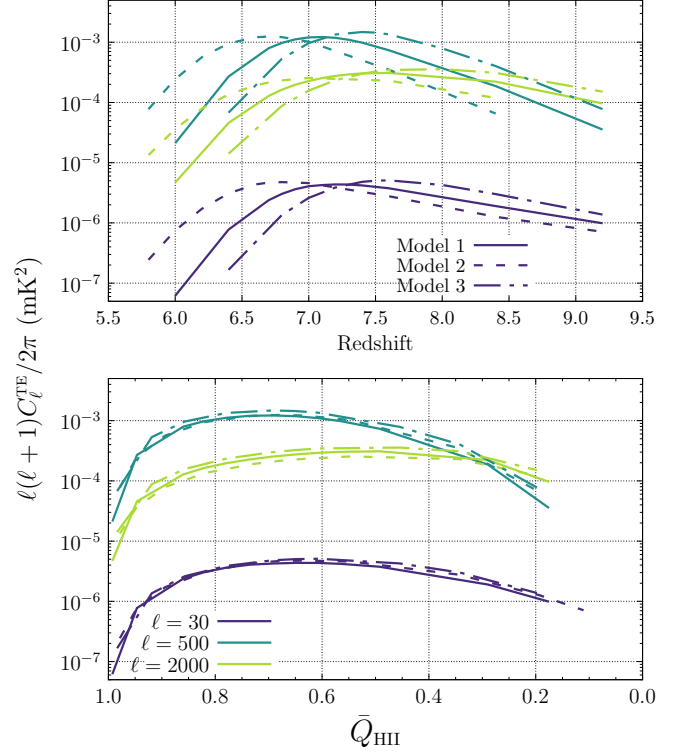


**Figure 8.** Same as Figure 7 but for the TE power spectrum  $C_\ell^{\text{TE}}$ . The results for  $\ell = 30$  are plotted with absolute values of  $C_\ell^{\text{TE}}$  since they are negative.

and  $C_\ell^{\text{TE}}/C_{\ell,\text{max}}^{\text{TE}}$ , where  $C_{\ell,\text{max}}^{\text{EE}}$  ( $C_{\ell,\text{max}}^{\text{TE}}$ ) is the maximum value of  $C_\ell^{\text{EE}}$  ( $C_\ell^{\text{TE}}$ ) during the EoR for a given  $\ell$ . We find that the full width at half maximum (FWHM) of the signal over the EoR is also insensitive to the ionization history, e.g. the FWHM of the power at  $\ell = 500$  approximately spans the range from  $\bar{Q}_{\text{HII}} = 0.50$  to  $0.90$ . In other words, the polarization signal (analyzed using  $C_\ell^{\text{TE}}$  and  $C_\ell^{\text{EE}}$ ) from the EoR can be observed over a broad redshift (frequency) range —  $\Delta z \sim 1$  ( $\Delta \nu_{\text{obs}} \sim 30$  MHz) in terms of the FWHM — regardless of the global ionization history, once the polarization measurement becomes feasible.

The top panels of Figures 7 and 8 show that the powers are highly model-dependent at a given redshift. However, since the reionization history varies with different models, if we compare the powers at a given global ionized fraction  $\bar{Q}_{\text{HII}}$ , we find that both powers show better convergence across different models in terms of their trends, and variations mostly appear in the overall amplitude only. Inspired by this finding, we plot the ratio  $C_\ell^{\text{EE}}/C_{\ell,\text{max}}^{\text{EE}}$  and  $C_\ell^{\text{TE}}/C_{\ell,\text{max}}^{\text{TE}}$  as function of  $\bar{Q}_{\text{HII}}$  in Figure 9, and find that the relations of these ratios and  $\bar{Q}_{\text{HII}}$  indeed show even better model-independence, for all three representative angular scales  $\ell$ . If the polarization measurement would be technically achievable, then

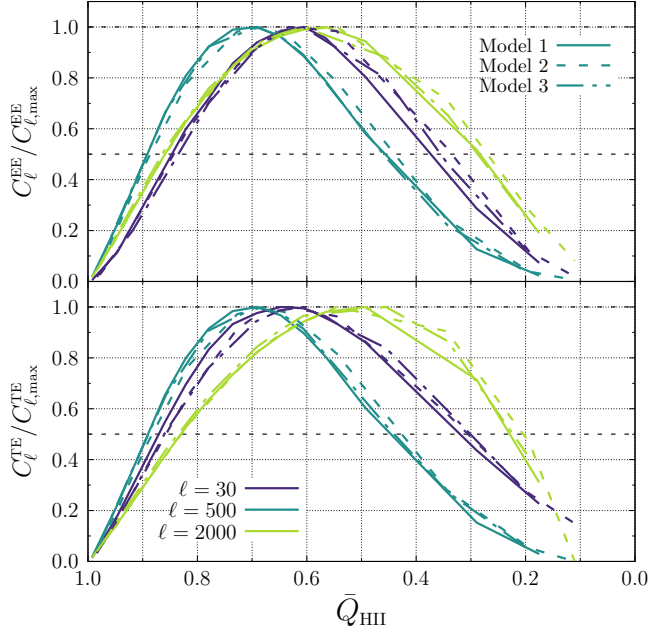


**Figure 9.** The ratio  $C_\ell^{\text{EE}}/C_{\ell,\text{max}}^{\text{EE}}$  (top) and  $C_\ell^{\text{TE}}/C_{\ell,\text{max}}^{\text{TE}}$  (bottom) as a function of the global H II volume filling fraction, for different Model 1/2/3 (solid/dashed/dot-dashed line) at different angular scales  $\ell = 30/500/2000$  (purple/dark green/light green). In the bottom panel, the ratios at  $\ell = 30$  are plotted with absolute values of  $C_\ell^{\text{TE}}$  since they are negative.

the robust mapping between the polarization signal and the global ionized fraction can be exploited to infer  $\bar{Q}_{\text{HII}}$  from the  $C_\ell^{\text{EE}}$  or  $C_\ell^{\text{TE}}$  measurements, thereby extracting at least some part of the reionization history in later stages of the EoR.

In short summary, our results show that the polarization of redshifted 21 cm lines can potentially probe large-scale spatial fluctuations of the IGM as well as the late-stage ionization history. In the next section we will discuss the prospects of its detection by upcoming intensity mapping experiments like SKA1-low.

## 5. DETECTION PROSPECTS

The temperature signal has hitherto been the focus of most 21 cm intensity mapping experiments. Particularly, in interferometer settings, the chief data product is the Stokes  $I$  visibility measured by each baseline (the cross-correlation between data from each pair of antennae/stations). However, by design those antennae are sensitive to polarization as well. In principle, we can construct visibilities for Stokes  $Q$ ,  $U$  and  $V$  of the true sky for interferometer arrays. The polarization signals themselves have long been sought with a variety of science goals (Heald et al. 2020). Nevertheless, a practical measurement of the polarization signal may be too am-

bitious a goal for current-generation instruments, due to several observational concerns with respect to uncertainties in 21 cm polarization measurements:

- (1) Instrumental calibration for polarization signal is more challenging than the calibration for temperature signal (e.g., Sault et al. 1996; Lenc et al. 2017).
- (2) Since radio foregrounds are intrinsically polarized, e.g. from the Galactic synchrotron emission (Kogut et al. 2007), we expect that those radio foregrounds can contaminate polarization measurements, too.
- (3) Besides foregrounds, the imperfect response of the primary beam to polarization is another major challenge for polarization observations to date. In fact, imperfect beams lead to biased measurements of the intensity signal in the meantime; if dipole antennae are not exactly identical or orthogonal for the two at the same location, there will be an entanglement between intensity and polarization in the observed  $I$  visibility, resulting in leakage of some of the polarization power into intensity.

Currently in 21 cm cosmology studies, observational attention to polarization is mainly concerned with this instrumental systematics in intensity measurements (e.g., Asad et al. 2018), rather than measuring the 21 cm polarization signal itself.

- (4) Although instrumental noise in different antennae are typically thought of as independent, correlations can still occur for neighboring ones, thus leading to a noise bias in the Stokes visibility data.
- (5) Probably the most worrying systematics result from the Faraday rotation (FR) effect, an effect that the polarization of radiation is rotated by intervening magnetic fields of cosmic origins or in the ionosphere of the Earth. For high-redshift 21 cm observation, magnetic fields rotate the initial Stokes  $Q$  and  $U$  by an angle  $\Delta_\lambda = \phi_{\text{LoS}}\lambda^2$  (Burn 1966), where  $\lambda$  is the observed wavelength and  $\phi_{\text{LoS}}$  is the Faraday depth integrated along the LoS.  $\phi_{\text{LoS}}$  is usually obtained by rotation measure (RM) synthesis.

Both EoR studies and cosmic magnetism science call for exquisite correction for instrumental effects mentioned above. In the context of SKA and its pathfinders, Heald et al. (2020) (their §4.1) discussed the advances in calibration techniques which may overcome some of the instrumental systematics and ionospheric effects, eventually allowing for high fidelity full-Stokes image cubes across wide fields of view. With clean sky images we can expect to construct unbiased estimators for desired

angular power spectra of the polarization signal (e.g., [Alonso et al. 2019](#)).

Once instrumental calibration is done, we still need to mitigate (subtract or avoid) foreground contaminants, which dominate in all parts of the sky for polarization as well. In the case of the intensity signal, current methods for foregrounds removal are mostly based upon the assumption that they have smooth spectral dependence (e.g., [Di Matteo et al. 2002](#)) compared with tomographic 21 cm signals. For polarization, foregrounds are additionally subject to FR, as are the 21 cm EoR polarization signals. Rotation angles that depend on the frequency ( $\propto \nu^{-2}$ ) can reach many multiples of  $2\pi$  at low frequencies. Therefore, FR with large RM values leads to features in the polarization spectra of foregrounds (as opposed to their smooth intensity spectra), and meanwhile threatens the reconstruction of initial polarization signals even in absence of foregrounds ([De & Tashiro 2014](#)).

On the other hand, FR provides an avenue to study cosmic magnetic fields. By broadband observations and RM synthesis techniques, modern radio astronomy aims at producing high precision RM maps which resolve structure of magnetic fields along each LoS. In fact, SKA lists *magnetism* as one of its high priority objectives, and an RM grid survey is planned on the SKA1-mid telescope ([Johnston-Hollitt et al. 2015](#)). Hence, instead of a pessimistic point of view at Faraday-rotated polarization data, we argue that they may offer new approaches to separating foregrounds and reconstructing the signal at the same time, when combined with intensity data. Such a possibility is worth further scrutiny.

In this paper, we only demonstrate the detection sensitivity by the conventional estimate of the measurement noise—the rms noise fluctuation in the visibility of a fixed baseline in one frequency channel centered at  $\nu_{\text{obs},0}$  ([Rohlf & Wilson 2004](#)),

$$\Delta V^N = \frac{T_{\text{sys}}}{A_{\text{eff}}} \frac{\lambda_{\text{obs},0}^2}{\sqrt{\Delta \nu_{\text{obs},0} t_v}}, \quad (19)$$

where  $T_{\text{sys}}(\nu_{\text{obs},0})$  is the system temperature, which is the sum of the sky brightness temperature and the receiver temperature,  $A_{\text{eff}}$  is the effective collection area of one antenna/station,  $\Delta \nu_{\text{obs},0}$  is the bandwidth of the channel and  $t_v$  is the observation time in this channel.  $T_{\text{sys}}/A_{\text{eff}}$  characterizes the sensitivity of an antenna. In the case of SKA1-low, baselines are formed by pairs of stations and the zenith sensitivity within  $45^\circ$  for one station is  $A_{\text{eff}}/T_{\text{sys}} \approx 1.5 \text{ m}^2/\text{K}$  across relevant frequencies.

Our assumption of sensitivity follows the SKA1-low antenna selection book<sup>12</sup>.

For illustration, we consider a drift-scan survey with maximal sky coverage by SKA1-low. Ignoring details of the map-making process in practice, we estimate the measurement uncertainty of  $C_\ell$  by the angular power spectrum of  $\Delta V^N$ , following [Zaldarriaga et al. \(2004\)](#) and [Mondal et al. \(2020\)](#),

$$C_\ell^N \approx \frac{(2\pi)^2 (T_{\text{sys}}/A_{\text{eff}})^2 \lambda_{\text{obs},0}^2 A_{\text{total}}}{\Delta \nu_{\text{obs},0} t_0} \frac{1}{2N_p N_s^2}, \quad (20)$$

where  $t_0$  is the total observing time,  $N_p = 2$  is the number of polarizations,  $A_{\text{total}}$  is the total area covered by the array and  $N_s$  is the number of stations within the array. Eq. (20) assumes a roughly uniform coverage of Fourier space during the course of the survey, preserving a white noise. For this reason, we only take into account the “core” of the actual SKA1-low array within the radius of about 500 meters, inside which 224 stations are closely packed<sup>13</sup>. We take the bandwidth to be  $\Delta \nu_{\text{obs},0} = 0.13 \text{ MHz}$  (2304 bands in total within the 50 – 350 MHz full SKA1-low bandwidth) and consider a total observing time of 4096 hrs (e.g., 512 nights with 8hrs per night).

The resulted noise power spectra are shown (labeled as “System noise”) in Figure 10. For comparison, we also plot the angular power spectra from different ionization histories. For each ionization history, the output redshifts are chosen such that they nearly correspond to  $\bar{Q}_{\text{HII}} \approx 35\%$ ,  $65\%$  and  $95\%$ . Although the error estimate here is primitive, the conclusion for  $C_\ell^{\text{TT}}$  is similar to that from [Mondal et al. \(2020\)](#) who accounted for the LC effect, that given reasonable integration time SKA1-low may detect the temperature signal by a signal-to-noise ratio (SNR) of over 10. However, for  $C_\ell^{\text{TE}}$  and  $C_\ell^{\text{EE}}$ , the 21 cm polarization signal is still several orders of magnitude below the noise power. This conclusion still holds even if we relax the total observation time to  $t_0 = 20000 \text{ hrs}$  under the current design sensitivity of SKA1-low. This contrasts with the optimistic conclusion in BL05 because (1) the polarization signal from the EoR is overestimated at large scales in BL05, and (2) current design sensitivity of SKA1-low is much worse than the early illustration in BL05. Therefore, with the designed sensitivity of the current-generation interferometer array experiment, it is not feasible to measure the 21 cm polarization power spectrum. It is still possi-

<sup>12</sup> See the link at [SKA1-LOW\\_Antenna\\_Selection.pdf](#).

<sup>13</sup> These parameters are adopted from the recent revision of the SKA1 baseline design document (SKA-TEL-SKO-0001075).



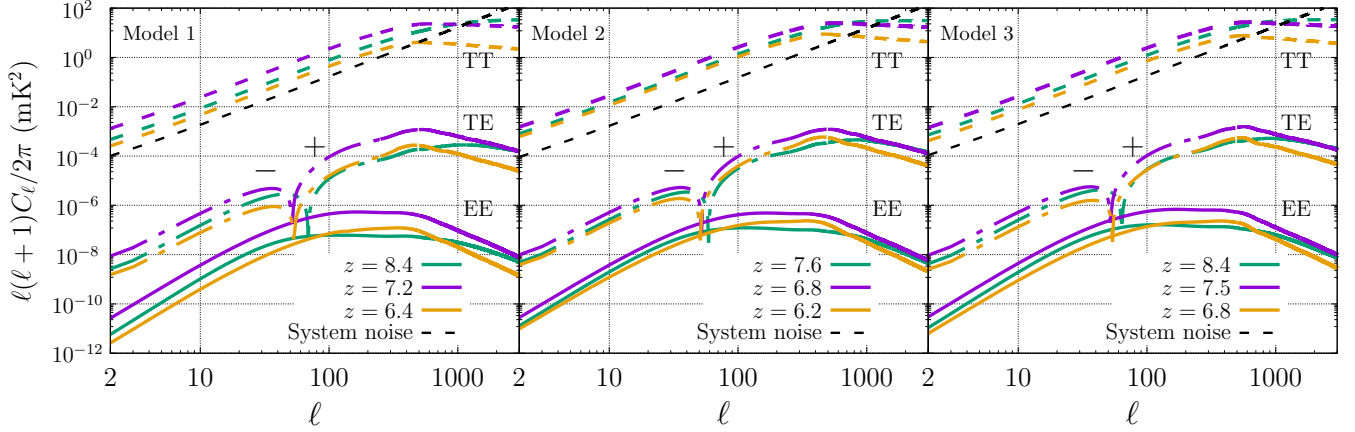


**Figure 10.** Angular power spectra of the 21 cm temperature (TT, dashed),  $E$ -mode polarization (EE, solid) and the temperature-polarization cross-correlation (TE, dot-dashed) from different Model 1/2/3 (left/middle/right panels). For each model (with different ionization history), shown are the results at various redshifts corresponding to  $\bar{Q}_{\text{HII}} \approx 35\%$  (green), 65% (purple) and 95% (yellow). TE power spectra are plotted with their absolute values, with the minus/plus sign marking the negative/positive part on the left/right-hand side of a sharp zero-crossing. The black dashed line represents an estimate of the system noise of an SKA1-low survey with total observing time of 4096 hrs. The frequency band of the noise power spectrum corresponds to the redshift of the largest signal shown in each panel.

ble, however, to consider its cross-correlation with other cosmic tracers.

## 6. SUMMARY

In this paper we reexamine the possibility of using the redshifted 21 cm polarization signal to probe cosmic reionization, in light of the upcoming H I intensity mapping surveys. For linearly polarized 21 cm lines due to Thomson scattering – the dominant mechanism for the 21 cm polarization signal – we improve the prediction of all-sky angular power spectra of the polarization autocorrelation and the temperature-polarization cross-correlation upon the previous work (BL05), by taking into account the nonlinear effect due to inhomogeneous reionization, and performing realistic modeling of patchy reionization with seminumerical simulations.

We find that both power spectra  $C_\ell^{\text{EE}}$  and  $C_\ell^{\text{TE}}$  are enhanced on the sub-bubble (i.e. small) scales, compared to the previous predictions from BL05. On the large scales, however, the peak amplitudes of both power spectra, which correspond to the characteristic scale of bubbles, are smaller than the BL05 results, partly due to the fact that our formalism includes the anti-correlation between the matter density field and the neutral fraction field. In particular, for all the global ionization histories considered herein,  $\sqrt{\ell(\ell+1)C_{\ell,\text{max}}^{\text{EE}}/2\pi}$  can only reach  $\sim 1 \mu\text{K}$  and  $\sqrt{\ell(\ell+1)C_{\ell,\text{max}}^{\text{TE}}/2\pi} \sim 0.03 \text{ mK}$ .

For the temperature-polarization cross-power spectrum, we find that  $C_\ell^{\text{TE}}$  flips its sign around  $\ell \simeq 50$ . The shape of  $C_\ell^{\text{TE}}$  is sensitive to the value of the linear H I bias on large scales during the EoR.

We demonstrate that the correlation between  $C_\ell/C_{\ell,\text{max}}$  and the global ionized fraction  $\bar{Q}_{\text{HII}}$ , for both EE and TE power spectra, is robust against the variation of reionization parameters. This correlation may be exploited to infer the global ionized fraction from the measurement of  $C_\ell/C_{\ell,\text{max}}$ , to reconstruct at least a part of reionization history from the midpoint to the late stages of the EoR.

Regarding the detectability of the 21 cm polarization signal, the thermal noise, foregrounds and systematics remain challenges to the observations. The problem of Faraday rotation may be resolved by future RM surveys, which may help the mitigation of polarization foreground, too. However, unlike the previous claim of BL05, even with FR corrected and foreground removed, the thermal noise in the polarization is still much larger than the signal in our new prediction, with the sensitivity of the SKA1-low telescope within reasonable integration time. Thus it might be more realistic to consider other approaches to extract the polarization information of 21 cm lines, e.g. likely through the cross-correlation of polarization with other cosmological probes.

## ACKNOWLEDGMENTS

This work is supported by National SKA Program of China (Grant No. 2020SKA0110401), NSFC (Grant No. 11821303), and National Key R&D Program of China (Grant No. 2018YFA0404502). We thank Shifan Zuo and Paulo Montero-Camacho for valuable comments and discussions. Numerical evaluations and simulations in this work were ran at the Venus cluster at the Tsinghua University.

## APPENDIX

## A. THE 21 CM BASICS: RELATIVISTIC FORMALISM

This appendix contains the full relativistic formalism for the 21 cm signal from the EoR which we omit in §2.1 and leads to the starting point of our calculation, Eq. (2). It closely follows those in Hall et al. (2013).

In Eq. (1), the 21 cm optical depth is given by the LoS integration (e.g., Lewis & Challinor 2007),

$$\tau_{\nu_{\text{obs}}} = \int_{\text{em}}^{\text{obs}} \frac{3h^3 A_{10} n_{\text{HI}}^g T_{21}}{32\pi p^g T_s^g} \phi(E^g - E_{21}) d\lambda, \quad (\text{A1})$$

where  $E^g = p^g c$  is the energy of the photon. The rest-frame 21 cm line profile  $\phi(E^g - E_{21})$  is defined such that  $\int \phi(E^g - E_{21}) dE^g = 1$ . It can be approximated as a Dirac delta function, hence simplifying the 21 cm optical depth:

$$\tau_{\nu_{\text{obs}}} = \frac{3h^3 c A_{10} T_{21} (1+z)}{32\pi E_{21}^2} \left( \frac{n_{\text{HI}}^g}{T_s^g} \left| \frac{d\lambda}{dz} \right| \right) \Big|_{\text{em}}, \quad (\text{A2})$$

where  $n_{\text{HI}}^g$  is the number density of the H I gas,  $\lambda$  is the affine parameter along the ray, and the subscript ‘em’ denotes the emission location where  $E^g(\lambda) = E_{21}$ . The (inverse) LoS differential redshift,  $|d\lambda/dz|$ , is attributed to the gravitational acceleration and the Doppler effect from the motion of the medium. It may diverge and thus cause  $\tau_{\nu_{\text{obs}}}$  to diverge, an extreme case due to the RSD component of the Doppler shift. However, for actual line profiles with finite width, the path integral in Eq. (A1) is always regular. Moreover, unlike the number count in galaxy redshift surveys, the brightness temperature given by Eq. (1) is always finite even when  $\tau_{\nu_{\text{obs}}}$  diverges (Mao et al. 2012).

The relationship between the gauge-invariant (GI) observed redshift and the gauge-dependent cosmological redshift is that, to linear order,

$$(1+z) \frac{a(\eta_{\text{em}})}{a(\eta_{\text{obs}})} = 1 + \hat{n} \cdot \left( \frac{\vec{v}_{\text{GI}}}{c} \right) \Big|_{\text{em}}^{\text{obs}} + \left( \frac{\Psi_A}{c^2} + \frac{\Phi_H}{c^2} - \frac{\Phi}{c^2} + \frac{1}{3} \nabla^2 E \right) \Big|_{\text{em}}^{\text{obs}} - \int_{\text{em}}^{\text{obs}} \left( \frac{\dot{\Psi}_A}{c^2} + \frac{\dot{\Phi}_H}{c^2} - \frac{c}{a} n^i n^j \partial_i \dot{V}_j + \frac{1}{2} n^i n^j \dot{h}_{ij} \right) d\eta = 1 + \frac{\delta z}{1+z}, \quad (\text{A3})$$

where the overdot denotes the partial time derivative with respect to  $\eta$ , the redshift variation  $\delta z \equiv 1+z-a(\eta_{\text{obs}})/a(\eta_{\text{em}})$ , and  $\Psi_A$ ,  $\Phi_H$ ,  $V_j$ ,  $h_{ij}$  are GI metric perturbations (Bardeen 1980; Bonvin & Durrer 2011). The GI velocity perturbation  $\vec{v}_{\text{GI}}$  is evaluated for both the observer and the emitting gas. It encodes the Doppler effect which sources the RSD.

In this paper, we have adopted the conformal Newtonian gauge ( $B = E = 0$ ,  $\Psi = \Psi_A$ ,  $\Phi = \Phi_H$ ) and only considered scalar perturbations. We have also assumed that the H I gas is pressureless. Therefore, according to the conservation of momentum,  $\dot{\vec{v}} + \mathcal{H}\vec{v} + \nabla\Psi = 0$ , where  $\vec{v}$  is the scalar-mode peculiar velocity of the gas.

## A.1. The 21 cm brightness temperature in the optically-thin, post-heating, quasi-linear regime

We have applied the following working assumptions throughout the paper:

- (1) 21 cm lines are optically thin,  $\tau_{\nu_{\text{obs}}} \ll 1$ , true for most ray paths (e.g., Lewis & Challinor 2007). It implies that  $dz/d\lambda < 0$  along the ray with respect to the emitting gas. Thus,  $z(\lambda)$  is monotonic (no ‘Finger-of-God’ effect). Also, we neglect the evolution of the ray direction along the photon geodesic so that it is always along  $\hat{n}$ .
- (2) The IGM has been preheated so that  $T_s^g(t_{\text{em}}) \gg (1+z)T_{\text{CMB}}^{\text{obs}}(\hat{n})$ . It is valid soon after reionization begins, when  $T_s^g$  quickly reaches above  $10^4$  K due to its coupling with the kinetic temperature of the gas via Lyman  $\alpha$  pumping (e.g., Chen & Miralda-Escudé 2004; Furlanetto 2006).
- (3) During the EoR, matter fluctuations are still Gaussian and linear on most relevant scales,  $|\delta| \ll 1$ , whereas H I density fluctuations are not, due to patchy reionization. This is the ‘quasi-linear’ regime in Mao et al. (2012).

These assumptions are the valid for most emitting H I gases during the EoR.

Putting everything together, the 21 cm brightness temperature for a fixed observer is given by, to linear order,

$$\begin{aligned}
\delta T_b(\eta_{\text{obs}}, \vec{x}, \nu_{\text{obs}}, \hat{n}) &\approx \frac{3h^3 c A_{10} T_{21} n_{\text{HI}}^g|_{\text{em}}}{32\pi E_{21}^2} \left| \frac{d\lambda}{dz} \right| \approx \frac{3c^3 A_{10} T_{21} n_{\text{HI}}^g|_{\text{em}}}{32\pi \nu_{21}^3 (1+z)} \left[ H(\eta) \left( 1 - \frac{\Psi}{c^2} \right) - \frac{1}{a} \frac{\dot{\Phi}}{c^2} + \frac{1}{a} \hat{n} \cdot (\hat{n} \cdot \nabla \vec{v}) \right]^{-1} \Big|_{\text{em}} \\
&= \frac{3c^3 A_{10} T_{21} n_{\text{HI}}^g|_{\text{em}}}{32\pi \nu_{21}^3 (1+z) H(\eta_{\text{em}})} \left( 1 - \frac{\Psi}{c^2} - \frac{1}{\mathcal{H}} \frac{\dot{\Phi}}{c^2} + \frac{1}{\mathcal{H}} \frac{\partial v_{\parallel}}{\partial r} \right)^{-1} \Big|_{\text{em}} \\
&\approx \frac{3c^3 A_{10} T_{21} \bar{n}_{\text{HI}}(\bar{\eta}_{z_{\text{em}}})}{32\pi \nu_{21}^3 (1+z) H(\bar{\eta}_{z_{\text{em}}})} \frac{(1 + \delta_{\text{HI}}|_{\text{em}}) \left( 1 + \frac{\dot{n}_{\text{HI}}}{\bar{n}_{\text{HI}}}(\bar{\eta}_{z_{\text{em}}}) \delta \eta_{\text{em}} \right)}{1 + \frac{\dot{H}}{H}(\bar{\eta}_{z_{\text{em}}}) \delta \eta_{\text{em}} + \left( \frac{1}{\mathcal{H}} \frac{\partial v_{\parallel}}{\partial r} - \frac{1}{\mathcal{H}} \frac{\dot{\Phi}}{c^2} - \frac{\Psi}{c^2} \right) \Big|_{\text{em}}}, \tag{A4}
\end{aligned}$$

where  $n_{\text{HI}}|_{\text{em}} \equiv \bar{n}_{\text{HI}}(\eta_{\text{em}})(1 + \delta_{\text{HI}}|_{\text{em}})$  defines the fluctuations of H I distribution on the hypersurface of  $\eta_{\text{em}}$ , and  $\delta \eta_{\text{em}} \equiv \eta_{\text{em}} - \bar{\eta}_{z_{\text{em}}}$ . Recall that  $1 + z_{\text{em}} \equiv (1+z)(1+z_{\text{obs}}) = \frac{1}{\langle a(\eta_{\text{em}}) \rangle}$ , defined in §2.1. The corresponding variation in the cosmological redshift can be defined as  $\delta z_{\text{em}} \equiv 1 + z_{\text{em}} - 1/a(\eta_{\text{em}})$ . We can show that  $\frac{\delta z_{\text{em}}}{1+z_{\text{em}}} = \mathcal{H}(z_{\text{em}}) \delta \eta_{\text{em}}$ . If the observer is on earth at the present,  $z_{\text{obs}} = 0$ ,  $z_{\text{em}} = z$  and  $\delta z_{\text{em}} = \delta z$ . Note that  $1 + z_{\text{em}} = \nu_{21}/\nu_{\text{obs},0}$ , even when the emission event is not on the past light cone of the present-day earth observer. Using Eq. (A3), we obtain the expression for the redshift variation in the Newtonian gauge,

$$\begin{aligned}
\frac{\delta z_{\text{em}}}{1+z_{\text{em}}} &= \frac{\delta z}{1+z} + \frac{\delta z_{\text{obs}}}{1+z_{\text{obs}}} = \left( \hat{n} \cdot \frac{\vec{v}}{c} + \frac{\Psi}{c^2} \right) \Big|_{\text{em}}^0 - \left( \int_{\text{em}}^{\text{obs}} + \int_{\text{obs}}^0 \right) \left( \frac{\dot{\Psi}}{c^2} + \frac{\dot{\Phi}}{c^2} \right) d\eta, \tag{A5} \\
\delta z_{\text{obs}} &\equiv z_{\text{obs}} - \tilde{z}_{\text{obs}}, \quad \langle \delta z_{\text{em}} \rangle = \langle \delta z \rangle = \langle \delta z_{\text{obs}} \rangle = 0, \quad \langle \delta \eta_{\text{em}} \rangle = \langle \delta \eta_{\text{obs}} \rangle = 0.
\end{aligned}$$

Eq. (A4) is the full relativistic expression for the 21 cm brightness temperature in the optically-thin, post-heating, quasi-linear limit, in agreement with Eq. (18) in Hall et al. (2013). The numerator and the denominator in the third line correspond to the redshift density perturbation ( $\delta_z$  in Bonvin & Durrer 2011) and the perturbation in the LoS length element extended by the gas per redshift bin ( $|d\lambda/dz|$ ), respectively, both GI. Note that the optically-thin limit is implied in the quasi-linear regime, since the RSD term (the velocity gradient) in the denominator is the only factor that can possibly make  $\tau_{\nu_{\text{obs}}}$  diverge. Eq. (A4) also shows that  $(1+z)\delta T_b$  is constant along the ray for fixed emission event and direction, as expected by the conservation of the photon distribution function during free streaming.

#### A.2. The redshift-space expansion of the brightness temperature and peculiar velocity effects

21 cm photons seen by a fixed observer at a fixed redshift (Eq. [1]) are actually emitted from different distances for different directions on the observer's past light cone. This is the so-called light-cone (LC) effect, mainly caused by the peculiar velocity of the gas. The extra anisotropy from the LC effect poses a major computational challenge to directly using Eq. (A4) to obtain the observed 21 cm signal. Also, it breaks the azimuthal symmetry around any mode vector  $\vec{k}$  in harmonic analysis, different from the CMB case. Besides the LC effect, H I peculiar velocities give rise to the RSD effect in the 21 cm intensity signal, as we see in Eq. (A4). The RSD occurs in the LoS length element,  $|d\lambda/dz|$ , as part of the Jacobian between the real- and redshift-space coordinates<sup>14</sup>. These effects need to be accounted for.

Our approximate solution is to rewrite the expression from the redshift-space point of view, by its Taylor expansion around the GI coordinate  $(\bar{\eta}_{z_{\text{em}}}, \vec{x} - s\hat{n})$ , as described in §2.1. The comoving radial distance in the redshift space reads

$$s = \int_{z_{\text{obs}}}^{z_{\text{em}}} \frac{cd\tilde{z}}{H(\tilde{z})} = c(\bar{\eta}_{z_{\text{obs}}} - \bar{\eta}_{z_{\text{em}}}) = c\langle (\eta_{\text{obs}} - \eta_{\text{em}}) \rangle = r(\hat{n}, z) + \frac{c\delta z_{\text{em}}}{H(z_{\text{em}})} - \frac{c\delta z_{\text{obs}}}{H(z_{\text{obs}})} = \langle r(\hat{n}, z) \rangle. \tag{A6}$$

Eq. (A5) shows that  $|\delta z|/(1+z) \ll 1$  for most of the emitting patches during the EoR, so that the Taylor series up to linear order of  $\delta \eta$  and  $(s-r)$  should be a good approximation for the signal. Discarding the negligible contribution from metric perturbations (the Sachs-Wolfe and integrated Sachs-Wolfe effect) in Eq. (A5) yields

$$\delta \eta_{\text{em}} \approx \frac{1}{\mathcal{H}(z_{\text{em}})} \frac{v_{\parallel}}{c} \Big|_0^{\text{em}}, \quad s - r \approx \frac{v_{\parallel}}{\mathcal{H}} \Big|_{\text{obs}}^{\text{em}}. \tag{A7}$$

<sup>14</sup> The 1D distortion along the LoS in the intensity mapping case is thus distinct from the traditional RSD effect in galaxy surveys which occurs in the 3D volume element (Hall et al. 2013).

Throughout the paper we have dropped the contributions from the observer's site since they only affect the monopole and dipole of the observed anisotropy. Thus, we obtain the following expression for  $\Theta$  to linear order:

$$\begin{aligned}\Theta(\eta_{\text{obs}}, \vec{x}, \nu_{\text{obs}}, \hat{n}) &= \frac{n_{\text{HI}}|_{\text{em}}/\bar{n}_{\text{HI}}(z_{\text{em}})}{1 + \frac{\dot{H}}{H}(z_{\text{em}})\delta\eta_{\text{em}} + \left(\frac{1}{\mathcal{H}}\frac{\partial v_{\parallel}}{\partial r} - \frac{1}{\mathcal{H}}\frac{\dot{\Phi}}{c^2} - \frac{\Psi}{c^2}\right)|_{\text{em}}} - 1 \\ &\approx \delta_{\text{HI}} - \frac{1}{\mathcal{H}}\frac{\partial v_{\parallel}}{\partial r}\frac{n_{\text{HI}}}{\bar{n}_{\text{HI}}} - (s-r)\frac{\partial\delta_{\text{HI}}}{\partial r} + \left(\frac{\dot{n}_{\text{HI}}}{\bar{n}_{\text{HI}}} - \frac{\dot{H}}{H}\frac{n_{\text{HI}}}{\bar{n}_{\text{HI}}}\right)\delta\eta_{\text{em}} \\ &\approx \delta_{\text{HI}} - \frac{1}{\mathcal{H}}\frac{\partial v_{\parallel}}{\partial r}\frac{n_{\text{HI}}}{\bar{n}_{\text{HI}}} - \frac{\partial\delta_{\text{HI}}}{\partial r}\frac{v_{\parallel}}{\mathcal{H}} + \left[\frac{\dot{n}_{\text{HI}}}{\bar{n}_{\text{HI}}} - \left(\frac{\dot{\mathcal{H}}}{\mathcal{H}} - \mathcal{H}\right)\frac{n_{\text{HI}}}{\bar{n}_{\text{HI}}}\right]\frac{v_{\parallel}}{c\mathcal{H}},\end{aligned}\quad (\text{A8})$$

where all variables on the right-hand side of the last line above are evaluated at  $(\bar{\eta}_{z_{\text{em}}}, \vec{x} - s\hat{n})$ .

The expression above can be simplified using the conservation of hydrogen number,  $\dot{n}_{\text{H}} + \nabla \cdot (n_{\text{H}}\vec{v}) + 3(\mathcal{H} - \dot{\Phi}/c^2)n_{\text{H}} = 0$ , combined with the fact that  $n_{\text{HI}} = n_{\text{H}}x_{\text{HI}}$ . This leads to

$$\dot{n}_{\text{HI}} + \nabla \cdot (n_{\text{HI}}\vec{v}) + 3(\mathcal{H} - \dot{\Phi}/c^2)n_{\text{HI}} = n_{\text{H}}(\dot{x}_{\text{HI}} + \nabla \cdot (x_{\text{HI}}\vec{v})). \quad (\text{A9})$$

Inserting it into Eq. (A8) yields

$$\Theta(\eta_{\text{obs}}, \vec{x}, \nu_{\text{obs}}, \hat{n}) \approx \delta_{\text{HI}} - \frac{n_{\text{HI}}}{\bar{n}_{\text{HI}}}\frac{\partial_r v_{\parallel}}{\mathcal{H}} + \left[\frac{\dot{x}_{\text{HI}}}{\bar{x}_{\text{HI},\text{m}}} - \frac{c\partial_r n_{\text{HI}}}{\bar{n}_{\text{HI}}} - \left(\frac{\dot{\mathcal{H}}}{\mathcal{H}} + 2\mathcal{H}\right)\frac{n_{\text{HI}}}{\bar{n}_{\text{HI}}}\right]\frac{v_{\parallel}}{c\mathcal{H}}, \quad (\text{A10})$$

where the second term on the right-hand side accounts for the RSD and the third term for the LC effect.

Figure 1 in Hall et al. (2013) shows that at low redshifts ( $z \sim 1-2$ ), the RSD is the dominant effect compared with the LC effect and metric perturbation terms in the full expression (A4). In this paper we have also neglected the LC and relativistic effects for the EoR signal, only keeping the RSD term, though the former may cause a change of the signal by a factor of order unity (Chapman & Santos 2019).

## B. GENERAL EXPRESSIONS FOR TEMPERATURE AND POLARIZATION ANGULAR POWER SPECTRA

In §2.2 we derive the angular power spectra of 21 cm temperature and polarization anisotropies, based on the expression for the temperature fluctuations given by Eq. (5), where  $\Theta$  is apparently sourced by  $\delta_{\text{HI}}$  and  $\delta$ . Here we present expressions for the general case in which multiple cosmological fields source temperature fluctuations and each source has its own transfer function. Those source fields are required to be statistically homogeneous and isotropic, and the temperature transfer functions should satisfy the azimuthal symmetry around  $\hat{k}$ . In other words,  $\Theta(\eta_{\text{obs}}, \vec{k}, \nu_{\text{obs}}, \mu) = \sum_i S_i(\vec{k}, z_{\text{em}})T_i^{\text{T}}(\eta_{\text{obs}}, k, \nu_{\text{obs}}, \mu)$ , where  $S_i$  represent the initial conditions for the  $i$ -th source and  $T_i^{\text{T}}$  the temperature transfer functions.

The (equal-time) auto-power spectra and cross-power spectra of the initial source fields are given by  $\langle S_i^*(\vec{k})S_j(\vec{k}') \rangle = (2\pi)^3 P_i(k)\delta_{\text{D}}^{(3)}(\vec{k} - \vec{k}')$  and  $\langle S_i^*(\vec{k})S_j(\vec{k}') \rangle = (2\pi)^3 P_{ij}(k)\delta_{\text{D}}^{(3)}(\vec{k} - \vec{k}')$ . Also, for each source, we can define multipole moments of the temperature and polarization transfer functions,

$$T_{i,\ell}^{\text{T}}(\eta_{\text{obs}}, k, \nu_{\text{obs}}) \equiv \frac{1}{(-i)^\ell} \int_{-1}^1 \frac{d\mu}{2} \mathcal{P}_\ell(\mu) T_i^{\text{T}}(\eta_{\text{obs}}, k, \nu_{\text{obs}}, \mu), \quad (\text{B11})$$

$$\mathcal{T}_{i,\ell}^{\text{E}}(\eta_{\text{obs}}, k, \nu_{\text{obs}}) \equiv \frac{3}{4} \sqrt{\frac{(\ell+2)!}{(\ell-2)!}} \int_{\bar{\eta}_{z_{\text{em}}}}^{\bar{\eta}_{z_{\text{obs}}}} g(\eta') T_{i,2}^{\text{T}}(\eta', k, \nu') \frac{j_\ell[ck(\bar{\eta}_{z_{\text{obs}}} - \eta')]}{[ck(\bar{\eta}_{z_{\text{obs}}} - \eta')]^2} d\eta'. \quad (\text{B12})$$

Recall that  $1 + z_{\text{em}} = (1+z)(1+z_{\text{obs}})$  and  $z$  is the observed (relative) redshift.

Hence, the angular power spectra of temperature and  $E$ -mode polarization anisotropies, for a generic observer located at  $(\eta_{\text{obs}}, \vec{x})$  and observing at frequency  $\nu_{\text{obs}}$ , are expressed as

$$C_\ell^{\text{EE}} = \frac{2}{\pi} \int k^2 dk \left[ \sum_i P_i(k, z_{\text{em}}) (\mathcal{T}_{i,\ell}^{\text{E}}(\eta_{\text{obs}}, k, \nu_{\text{obs}}))^2 + \sum_{i \neq j} P_{ij}(k, z_{\text{em}}) \mathcal{T}_{i,\ell}^{\text{E}}(\eta_{\text{obs}}, k, \nu_{\text{obs}}) \mathcal{T}_{j,\ell}^{\text{E}}(\eta_{\text{obs}}, k, \nu_{\text{obs}}) \right], \quad (\text{B13})$$

$$C_\ell^{\text{TT}} = \frac{2}{\pi} \int k^2 dk \left[ \sum_i P_i(k, z_{\text{em}}) (T_{i,\ell}(\eta_{\text{obs}}, k, \nu_{\text{obs}}))^2 + \sum_{i \neq j} P_{ij}(k, z_{\text{em}}) T_{i,\ell}(\eta_{\text{obs}}, k, \nu_{\text{obs}}) T_{j,\ell}(\eta_{\text{obs}}, k, \nu_{\text{obs}}) \right]. \quad (\text{B14})$$

The cross-power spectrum between the temperature and the  $E$ -mode polarization is

$$C_{\ell}^{\text{TE}} = \frac{2}{\pi} \int k^2 dk \left[ \sum_i P_i(k, z_{\text{em}}) T_{i,\ell}(\eta_{\text{obs}}, k, \nu_{\text{obs}}) \mathcal{T}_{i,\ell}^{\text{E}}(\eta_{\text{obs}}, k, \nu_{\text{obs}}) + \sum_{i \neq j} P_{ij}(k, z_{\text{em}}) T_{i,\ell}(\eta_{\text{obs}}, k, \nu_{\text{obs}}) \mathcal{T}_{j,\ell}^{\text{E}}(\eta_{\text{obs}}, k, \nu_{\text{obs}}) \right]. \quad (\text{B15})$$

## REFERENCES

- Ahn, K., Xu, H., Norman, M. L., Alvarez, M. A., & Wise, J. H. 2015, *ApJ*, 802, 8, doi: [10.1088/0004-637X/802/1/8](https://doi.org/10.1088/0004-637X/802/1/8)
- Alonso, D., Sanchez, J., Slosar, A., & LSST Dark Energy Science Collaboration. 2019, *MNRAS*, 484, 4127, doi: [10.1093/mnras/stz093](https://doi.org/10.1093/mnras/stz093)
- Asad, K. M. B., Koopmans, L. V. E., Jelić, V., et al. 2018, *MNRAS*, 476, 3051, doi: [10.1093/mnras/sty258](https://doi.org/10.1093/mnras/sty258)
- Aubert, D., Deparis, N., & Ocvirk, P. 2015, *MNRAS*, 454, 1012, doi: [10.1093/mnras/stv1896](https://doi.org/10.1093/mnras/stv1896)
- Babich, D., & Loeb, A. 2005, *ApJ*, 635, 1, doi: [10.1086/497297](https://doi.org/10.1086/497297)
- Bardeen, J. M. 1980, *PhRvD*, 22, 1882, doi: [10.1103/PhysRevD.22.1882](https://doi.org/10.1103/PhysRevD.22.1882)
- Barkana, R., & Loeb, A. 2005, *ApJL*, 624, L65, doi: [10.1086/430599](https://doi.org/10.1086/430599)
- Becker, G. D., Bolton, J. S., Madau, P., et al. 2015, *MNRAS*, 447, 3402, doi: [10.1093/mnras/stu2646](https://doi.org/10.1093/mnras/stu2646)
- Bharadwaj, S., & Ali, S. S. 2004, *MNRAS*, 352, 142, doi: [10.1111/j.1365-2966.2004.07907.x](https://doi.org/10.1111/j.1365-2966.2004.07907.x)
- Bonvin, C., & Durrer, R. 2011, *PhRvD*, 84, 063505, doi: [10.1103/PhysRevD.84.063505](https://doi.org/10.1103/PhysRevD.84.063505)
- Bouwens, R. J., Illingworth, G. D., Oesch, P. A., et al. 2015, *ApJ*, 811, 140, doi: [10.1088/0004-637X/811/2/140](https://doi.org/10.1088/0004-637X/811/2/140)
- Bowman, J. D., Rogers, A. E. E., Monsalve, R. A., Mozdzen, T. J., & Mahesh, N. 2018, *Nature*, 555, 67, doi: [10.1038/nature25792](https://doi.org/10.1038/nature25792)
- Brentjens, M. A., & de Bruyn, A. G. 2005, *A&A*, 441, 1217, doi: [10.1051/0004-6361:20052990](https://doi.org/10.1051/0004-6361:20052990)
- Brown, S., Bergerud, B., Costa, A., et al. 2019, *MNRAS*, 483, 964, doi: [10.1093/mnras/sty2908](https://doi.org/10.1093/mnras/sty2908)
- Burn, B. J. 1966, *MNRAS*, 133, 67, doi: [10.1093/mnras/133.1.67](https://doi.org/10.1093/mnras/133.1.67)
- Chapman, E., & Santos, M. G. 2019, *MNRAS*, 490, 1255, doi: [10.1093/mnras/stz2663](https://doi.org/10.1093/mnras/stz2663)
- Chen, X., & Miralda-Escudé, J. 2004, *ApJ*, 602, 1, doi: [10.1086/380829](https://doi.org/10.1086/380829)
- Chen, Z., Xu, Y., Wang, Y., & Chen, X. 2019, *ApJ*, 885, 23, doi: [10.3847/1538-4357/ab43e6](https://doi.org/10.3847/1538-4357/ab43e6)
- Cooray, A., & Furlanetto, S. R. 2005, *MNRAS*, 359, L47, doi: [10.1111/j.1745-3933.2005.00035.x](https://doi.org/10.1111/j.1745-3933.2005.00035.x)
- Datta, K. K., Choudhury, T. R., & Bharadwaj, S. 2007, *MNRAS*, 378, 119, doi: [10.1111/j.1365-2966.2007.11747.x](https://doi.org/10.1111/j.1365-2966.2007.11747.x)
- De, S., & Tashiro, H. 2014, *PhRvD*, 89, 123002, doi: [10.1103/PhysRevD.89.123002](https://doi.org/10.1103/PhysRevD.89.123002)
- DeBoer, D. R., Parsons, A. R., Aguirre, J. E., et al. 2017, *PASP*, 129, 045001, doi: [10.1088/1538-3873/129/974/045001](https://doi.org/10.1088/1538-3873/129/974/045001)
- Di Matteo, T., Perna, R., Abel, T., & Rees, M. J. 2002, *ApJ*, 564, 576, doi: [10.1086/324293](https://doi.org/10.1086/324293)
- Dixon, K. L., Iliev, I. T., Mellema, G., Ahn, K., & Shapiro, P. R. 2016, *MNRAS*, 456, 3011, doi: [10.1093/mnras/stv2887](https://doi.org/10.1093/mnras/stv2887)
- Fan, X., Strauss, M. A., Becker, R. H., et al. 2006, *AJ*, 132, 117, doi: [10.1086/504836](https://doi.org/10.1086/504836)
- Finkelstein, S. L., D'Aloisio, A., Paardekoooper, J.-P., et al. 2019, *ApJ*, 879, 36, doi: [10.3847/1538-4357/ab1ea8](https://doi.org/10.3847/1538-4357/ab1ea8)
- Furlanetto, S. R. 2006, *MNRAS*, 371, 867, doi: [10.1111/j.1365-2966.2006.10725.x](https://doi.org/10.1111/j.1365-2966.2006.10725.x)
- Furlanetto, S. R., Zaldarriaga, M., & Hernquist, L. 2004a, *ApJ*, 613, 16, doi: [10.1086/423028](https://doi.org/10.1086/423028)
- . 2004b, *ApJ*, 613, 1, doi: [10.1086/423025](https://doi.org/10.1086/423025)
- Greig, B., & Mesinger, A. 2017, *MNRAS*, 465, 4838, doi: [10.1093/mnras/stw3026](https://doi.org/10.1093/mnras/stw3026)
- Gruzinov, A., & Hu, W. 1998, *ApJ*, 508, 435, doi: [10.1086/306432](https://doi.org/10.1086/306432)
- Hall, A., Bonvin, C., & Challinor, A. 2013, *PhRvD*, 87, 064026, doi: [10.1103/PhysRevD.87.064026](https://doi.org/10.1103/PhysRevD.87.064026)
- Heald, G., Mao, S., Vacca, V., et al. 2020, *Galaxies*, 8, 53, doi: [10.3390/galaxies8030053](https://doi.org/10.3390/galaxies8030053)
- Hirata, C. M., Mishra, A., & Venumadhav, T. 2018, *PhRvD*, 97, 103521, doi: [10.1103/PhysRevD.97.103521](https://doi.org/10.1103/PhysRevD.97.103521)
- Hoffmann, K., Mao, Y., Xu, J., Mo, H., & Wandelt, B. D. 2019, *MNRAS*, 487, 3050, doi: [10.1093/mnras/stz1472](https://doi.org/10.1093/mnras/stz1472)
- Hu, W. 2000, *ApJ*, 529, 12, doi: [10.1086/308279](https://doi.org/10.1086/308279)
- Hutschenreuter, S., & Enßlin, T. A. 2020, *A&A*, 633, A150, doi: [10.1051/0004-6361/201935479](https://doi.org/10.1051/0004-6361/201935479)
- Iliev, I. T., Mellema, G., Ahn, K., et al. 2014, *MNRAS*, 439, 725, doi: [10.1093/mnras/stt2497](https://doi.org/10.1093/mnras/stt2497)
- Ji, L., Kamionkowski, M., & Inomata, K. 2021, *PhRvD*, 103, 023516, doi: [10.1103/PhysRevD.103.023516](https://doi.org/10.1103/PhysRevD.103.023516)
- Johnston-Hollitt, M., Govoni, F., Beck, R., et al. 2015, in *Advancing Astrophysics with the Square Kilometre Array (AASKA14)*, 92. <https://arxiv.org/abs/1506.00808>



- Knox, L., Scoccimarro, R., & Dodelson, S. 1998, *PhRvL*, 81, 2004, doi: [10.1103/PhysRevLett.81.2004](https://doi.org/10.1103/PhysRevLett.81.2004)
- Kogut, A., Dunkley, J., Bennett, C. L., et al. 2007, *ApJ*, 665, 355, doi: [10.1086/519754](https://doi.org/10.1086/519754)
- Koopmans, L., Pritchard, J., Mellema, G., et al. 2015, in *Advancing Astrophysics with the Square Kilometre Array (AASKA14)*, 1. <https://arxiv.org/abs/1505.07568>
- Lenc, E., Anderson, C. S., Barry, N., et al. 2017, *PASA*, 34, e040, doi: [10.1017/pasa.2017.36](https://doi.org/10.1017/pasa.2017.36)
- Lewis, A., & Challinor, A. 2007, *PhRvD*, 76, 083005, doi: [10.1103/PhysRevD.76.083005](https://doi.org/10.1103/PhysRevD.76.083005)
- Lidz, A., Zahn, O., McQuinn, M., Zaldarriaga, M., & Hernquist, L. 2008, *ApJ*, 680, 962, doi: [10.1086/587618](https://doi.org/10.1086/587618)
- Liu, A., & Shaw, J. R. 2020, *PASP*, 132, 062001, doi: [10.1088/1538-3873/ab5bfd](https://doi.org/10.1088/1538-3873/ab5bfd)
- Liu, A., Zhang, Y., & Parsons, A. R. 2016, *ApJ*, 833, 242, doi: [10.3847/1538-4357/833/2/242](https://doi.org/10.3847/1538-4357/833/2/242)
- Madau, P., Meiksin, A., & Rees, M. J. 1997, *ApJ*, 475, 429, doi: [10.1086/303549](https://doi.org/10.1086/303549)
- Majumdar, S., Mellema, G., Datta, K. K., et al. 2014, *MNRAS*, 443, 2843, doi: [10.1093/mnras/stu1342](https://doi.org/10.1093/mnras/stu1342)
- Mao, Y., Shapiro, P. R., Mellema, G., et al. 2012, *MNRAS*, 422, 926, doi: [10.1111/j.1365-2966.2012.20471.x](https://doi.org/10.1111/j.1365-2966.2012.20471.x)
- Mao, Y., Tegmark, M., McQuinn, M., Zaldarriaga, M., & Zahn, O. 2008, *PhRvD*, 78, 023529, doi: [10.1103/PhysRevD.78.023529](https://doi.org/10.1103/PhysRevD.78.023529)
- McGreer, I. D., Mesinger, A., & D’Odorico, V. 2015, *MNRAS*, 447, 499, doi: [10.1093/mnras/stu2449](https://doi.org/10.1093/mnras/stu2449)
- McQuinn, M., Zahn, O., Zaldarriaga, M., Hernquist, L., & Furlanetto, S. R. 2006, *ApJ*, 653, 815, doi: [10.1086/505167](https://doi.org/10.1086/505167)
- Mesinger, A., Furlanetto, S., & Cen, R. 2011, *MNRAS*, 411, 955, doi: [10.1111/j.1365-2966.2010.17731.x](https://doi.org/10.1111/j.1365-2966.2010.17731.x)
- Mondal, R., Bharadwaj, S., & Datta, K. K. 2018, *MNRAS*, 474, 1390, doi: [10.1093/mnras/stx2888](https://doi.org/10.1093/mnras/stx2888)
- Mondal, R., Shaw, A. K., Iliev, I. T., et al. 2020, *MNRAS*, 494, 4043, doi: [10.1093/mnras/staa1026](https://doi.org/10.1093/mnras/staa1026)
- Morales, M. F., & Hewitt, J. 2004, *ApJ*, 615, 7, doi: [10.1086/424437](https://doi.org/10.1086/424437)
- O’Sullivan, S. P., Brüggén, M., Vazza, F., et al. 2020, *MNRAS*, 495, 2607, doi: [10.1093/mnras/staa1395](https://doi.org/10.1093/mnras/staa1395)
- Planck Collaboration, Aghanim, N., Akrami, Y., et al. 2020, *A&A*, 641, A6, doi: [10.1051/0004-6361/201833910](https://doi.org/10.1051/0004-6361/201833910)
- Pritchard, J. R., & Loeb, A. 2012, *Reports on Progress in Physics*, 75, 086901, doi: [10.1088/0034-4885/75/8/086901](https://doi.org/10.1088/0034-4885/75/8/086901)
- Robertson, B. E., Ellis, R. S., Furlanetto, S. R., & Dunlop, J. S. 2015, *ApJL*, 802, L19, doi: [10.1088/2041-8205/802/2/L19](https://doi.org/10.1088/2041-8205/802/2/L19)
- Rohlf, K., & Wilson, T. L. 2004, *Tools of radio astronomy*
- Santos, M. G., Ferramacho, L., Silva, M. B., Amblard, A., & Cooray, A. 2010, *MNRAS*, 406, 2421, doi: [10.1111/j.1365-2966.2010.16898.x](https://doi.org/10.1111/j.1365-2966.2010.16898.x)
- Sault, R. J., Hamaker, J. P., & Bregman, J. D. 1996, *A&AS*, 117, 149
- Scott, D., & Rees, M. J. 1990, *MNRAS*, 247, 510
- Wyithe, J. S. B., & Loeb, A. 2004, *Nature*, 427, 815, doi: [10.1038/nature02336](https://doi.org/10.1038/nature02336)
- Zaldarriaga, M., Furlanetto, S. R., & Hernquist, L. 2004, *ApJ*, 608, 622, doi: [10.1086/386327](https://doi.org/10.1086/386327)
- Zaldarriaga, M., & Seljak, U. 1997, *PhRvD*, 55, 1830, doi: [10.1103/PhysRevD.55.1830](https://doi.org/10.1103/PhysRevD.55.1830)